# A stable second-order scheme for fluid–structure interaction with strong added-mass effects

Jie Liu [a], Rajeev K. Jaiman [b,*], Pardha S. Gurugubelli [b]

[a] Department of Mathematics, National University Singapore, Singapore
[b] Department of Mechanical Engineering, National University Singapore, Singapore

A B S T R A C T

In this paper, we present a stable second-order time accurate scheme for solving fluid–structure interaction problems. The scheme uses so-called Combined Field with Explicit Interface (CFEI) advancing formulation based on the Arbitrary Lagrangian–Eulerian approach with finite element procedure. Although loosely-coupled partitioned schemes are often popular choices for simulating FSI problems, these schemes may suffer from inherent instability at low structure to fluid density ratios. We show that our second-order scheme is stable for any mass density ratio and hence is able to handle strong added-mass effects. Energy-based stability proof relies heavily on the connections among extrapolation formula, trapezoidal scheme for second-order equation, and backward difference method for first-order equation.

Numerical accuracy and stability of the scheme is assessed with the aid of two-dimensional fluid–structure interaction problems of increasing complexity. We confirm second-order temporal accuracy by numerical experiments on an elastic semi-circular cylinder problem. We verify the accuracy of coupled solutions with respect to the benchmark solutions of a cylinder-elastic bar and the Navier–Stokes flow system. To study the stability of the proposed scheme for strong added-mass effects, we present new results using the combined field formulation for flexible flapping motion of a thin-membrane structure with low mass ratio and strong added-mass effects in a uniform axial flow. Using a systematic series of fluid–structure simulations, a detailed analysis of the coupled response as a function of mass ratio for the case of very low bending rigidity has been presented.

© 2014 Elsevier Inc. All rights reserved.

## 1. Introduction

A stable and efficient numerical technique is essential for the study of nonlinear fluid–structure interaction (FSI) problems in the fields of aerospace [1,2], bio-engineering [3,4], civil and offshore engineering [5,6]. Two main categories of methods are available, which differ on their treatment of fluid–structure interface. In the first category, a discrete version of the interface moves in a non-conformal manner across a fixed mesh in space. This requires an additional property to capture the interface such as a level set function [7], an immersed structure [4,8], a Lagrange multiplier, fictitious domains or ghost fluid [9,10]. In the second category, both the interface and mesh in space move together keeping conformity in a body-fitted manner. The arbitrary Lagrangian–Eulerian (ALE) approach [11,12] was introduced to handle the time derivative terms on

* Corresponding author.
  *E-mail address:* mperkj@nus.edu.sg (R.K. Jaiman).

the time-varying fluid domain. It prevents excessive mesh distortion comparing with the pure Lagrangian approach. The capability to design high order methods makes methods of the second category of great interest for practical problems.

The ALE based FSI simulations are generally accomplished by using either partitioned or monolithic schemes. A monolithic [13–16] approach assembles the fluid and structural equations into a single block and solves them simultaneously for each iteration. These schemes lack the advantage of flexibility and modularity of using existing stable fluid or structural solvers. However, they offer good numerical stability even for problems involving very strong added mass effects. In contrast, a partitioned approach solves the fluid and structural equations in a sequential manner, facilitating the coupling of the existing fluid and structural program with minimal changes. This trait of the partitioned approach therefore makes itself an attractive option from computational point of view.

Typically, partitioned staggered schemes [17] are classified as either strongly-coupled [18] or loosely-coupled [19,20]. Loosely-coupled schemes satisfy the interface velocity continuity and traction continuity conditions in a sequential manner. These schemes often suffer from numerical instability and temporal inaccuracy caused by spurious energy production along the interface due to the time lag [21,22], and special treatments are generally required to address these issues. A variety of force corrections and structural predictors [19,23] are used to increase the numerical stability of loosely-coupled schemes. Strongly-coupled schemes typically involve predictor–corrector sub-iterations to ensure the convergence of interface properties. However, this results in increased computational cost. In several applications such as, flow through blood vessels [24], ocean current interactions with offshore risers [6], strongly-coupled schemes suffer from convergence issues due to strongly predominant added mass effects [25].

The key objective of this paper is to present an efficient second-order scheme to solve the fully coupled FSI problems which is stable for any mass density ratio. We further present an energy based stability proof for the proposed second order scheme. The scheme is based on the combined field formulation proposed in [26] which uses the ALE description for the fluid and Lagrangian description for the solid. The combined field scheme presented in [26] is first-order accurate and is motivated by the one-fluid formulation [27] for studying multiphase problems. There is no systematic study on the effects of mass ratio in the earlier work presented in [26].

The CFEI formulation is based on weak formulation of fluid–structure problem with properly chosen function spaces for the unknown variables. Both governing equations for fluid and solid are written in terms of their velocities, respectively. Solid position plays only a role of slave variable. The continuity of velocities across the fluid–structure interface is enforced in the function spaces, while the continuity of traction across the interface is enforced in the weak formulation. The definition of the function space for the velocities requires information on the solid position. Since the solid position is also an unknown quantity, decoupling of the computations of the solid position and the remaining variables is performed in this weak formulation. In the CFEI formulation, this requirement automatically leads to an explicit interface advancing for updating the solid positions and handling mesh velocity in the ALE formulation of the Navier–Stokes equations. This explicit advancing of the mesh velocity in turn requires an explicit treatment of the convective velocity in the quadratic term of the Navier–Stokes equations to achieve a desired energy balance. The other velocity in the quadratic terms is treated implicitly and this semi-implicit treatment is crucial for the stability proof as shown in [26]. Another important consequence of the semi-implicit treatment is that the CFEI formulation only requires to solve a linear system of equations per time step.

The proposed CFEI scheme is unconditionally stable with respect to mass ratios with relatively lesser number of unknowns compared to the traditional monolithic schemes. The energy-based stability proof for the second-order fully discrete scheme proposed in this paper relies heavily on the CFEI formulation and on the connections among the second-order extrapolation formula, the backward differentiation, and the trapezoidal rule. The numerical scheme preserves the energy decaying property for a fluid–structure system. The temporal accuracy of the CFEI scheme has been assessed with the aid of 2D incompressible flow interacting with structure. We show the second-order temporal accuracy for a test problem on elastic semi-circular cylinder and verify the precision with the benchmark results for the cylinder-elastic bar problem. Furthermore, we use this CFEI scheme to study the flapping dynamics involving low mass density ratio and bending rigidity modulus.

The content of this paper is organized as follows. In Section 2, we start with the governing equations used to model the FSI problem and a review of the CFEI formulation has been presented. Section 3 presents the scheme with second-order accuracy in time. The stability of the scheme is proved in Section 4. In Section 5, we present the convergence and verification results. Section 6 presents the application of CFEI formulation to study the flapping dynamics of a thin structure in a uniform axial flow. The major conclusions of this work are reported in Section 7.

## 2. Combined field with explicit advancing

Before the presentation of our second-order scheme, we provide for completeness a short description of the fluid–structure system and the combined field formulation. The governing equations for the fluid are written in an ALE form while the structural equation is formulated in a Lagrangian way.

### 2.1. Fluid–structure equations

Let $\Omega^{\mathrm{f}}(t) \subset \mathbb{R}^d$ be a fluid domain at time $t$, where d is the space dimension. The motion of an incompressible viscous fluid in $\Omega^{\mathrm{f}}(t)$ is governed by the following Navier–Stokes equations:

$$\rho^{\mathrm{f}}\frac{\partial \boldsymbol{u}^{\mathrm{f}}}{\partial t} + \rho^{\mathrm{f}}\boldsymbol{u}^{\mathrm{f}}\cdot\nabla\boldsymbol{u}^{\mathrm{f}} = \nabla\cdot\boldsymbol{\sigma}^{\mathrm{f}} + \rho^{\mathrm{f}}\boldsymbol{g}^{\mathrm{f}} \quad \text{in } \Omega^{\mathrm{f}}(t), \tag{1}$$

$$\nabla\cdot\boldsymbol{u}^{\mathrm{f}} = 0 \quad \text{in } \Omega^{\mathrm{f}}(t). \tag{2}$$

Here $\rho^{\mathrm{f}}$, $\boldsymbol{u}^{\mathrm{f}}$, $\rho^{\mathrm{f}}\boldsymbol{g}^{\mathrm{f}}$ and $\boldsymbol{\sigma}^{\mathrm{f}}$ are the density, velocity, body force and Cauchy stress tensor of the fluid, respectively. The stress tensor is written as

$$\boldsymbol{\sigma}^{\mathrm{f}} = -p^{\mathrm{f}}\mathbf{I} + \boldsymbol{T}^{\mathrm{f}}, \quad \boldsymbol{T}^{\mathrm{f}} = 2\rho^{\mathrm{f}}\nu^{\mathrm{f}}\boldsymbol{\epsilon}^{\mathrm{f}}(\boldsymbol{u}^{\mathrm{f}}), \quad \boldsymbol{\epsilon}^{\mathrm{f}}(\boldsymbol{u}^{\mathrm{f}}) = \frac{1}{2}\big[\nabla\boldsymbol{u}^{\mathrm{f}} + (\nabla\boldsymbol{u}^{\mathrm{f}})^{T}\big], \tag{3}$$

where $p^{\mathrm{f}}$, $\mathbf{I}$, $\nu^{\mathrm{f}}$ and $\boldsymbol{\epsilon}^{\mathrm{f}}$ are the pressure, identity tensor, kinematic viscosity, and strain rate tensor of the fluid, respectively.

Let $\Omega^{\mathrm{s}} \subset \mathbb{R}^{d}$ be the reference domain for a flexible elastic structure. A material point, whose initial position is given by $\boldsymbol{z} \in \Omega^{\mathrm{s}}$, deforms to position $\boldsymbol{\varphi}^{\mathrm{s}}(\boldsymbol{z}, t)$ at time $t$ with the structural momentum equation

$$\rho^{\mathrm{s}}\frac{\partial^{2}\boldsymbol{\varphi}^{\mathrm{s}}}{\partial t^{2}} = \nabla\cdot\boldsymbol{\sigma}^{\mathrm{s}} + \boldsymbol{f}^{\mathrm{s}} \quad \text{in } \Omega^{\mathrm{s}}, \tag{4}$$

where $\boldsymbol{\sigma}^{\mathrm{s}}$ denotes the first Piola–Kirchhoff stress tensor, $\boldsymbol{f}^{\mathrm{s}}$ represents the body force vector acting on the structure, and $\rho^{\mathrm{s}}$ is its mass density. For a linear elastic material,

$$\boldsymbol{\sigma}^{\mathrm{s}}(\boldsymbol{\varphi}^{\mathrm{s}}) = \mu^{\mathrm{s}}\big[\nabla\boldsymbol{\eta}^{\mathrm{s}} + (\nabla\boldsymbol{\eta}^{\mathrm{s}})^{T}\big] + \lambda^{\mathrm{s}}(\nabla\cdot\boldsymbol{\eta}^{\mathrm{s}})\mathbf{I}, \tag{5}$$

where $\boldsymbol{\eta}^{\mathrm{s}}(\boldsymbol{z}, t) = \boldsymbol{\varphi}^{\mathrm{s}}(\boldsymbol{z}, t) - \boldsymbol{z}$ is the displacement vector, $\mu^{\mathrm{s}}$ and $\lambda^{\mathrm{s}}$ are the Lame's constants. For a St. Venant–Kirchhoff material,

$$\boldsymbol{\sigma}^{\mathrm{s}}(\boldsymbol{\varphi}^{\mathrm{s}}) = 2\mu^{\mathrm{s}}\boldsymbol{F}\boldsymbol{E} + \lambda^{\mathrm{s}}(\operatorname{tr}\boldsymbol{E})\boldsymbol{F}, \tag{6}$$

where $\boldsymbol{F}$ is the deformation tensor given as $\nabla\boldsymbol{\varphi}^{\mathrm{s}}$, and $\boldsymbol{E}$ represents the strain tensor

$$\boldsymbol{E} = \frac{1}{2}\big(\boldsymbol{F}\boldsymbol{F}^{T} - \mathbf{I}\big). \tag{7}$$

Before we present the weak form of the CFEI formulation, we rewrite (4) in terms of the structural velocity $\boldsymbol{u}^{\mathrm{s}}$, defined as

$$\boldsymbol{u}^{\mathrm{s}}(\boldsymbol{z}, t) = \partial_{t}\boldsymbol{\varphi}^{\mathrm{s}}(\boldsymbol{z}, t). \tag{8}$$

This modification creates the path for the implementation of the velocity continuity (i.e. kinematic matching) along the fluid–structure interface. The structural governing equation (4) can therefore be rewritten as

$$\rho^{\mathrm{s}}\frac{\partial \boldsymbol{u}^{\mathrm{s}}}{\partial t} = \nabla\cdot\boldsymbol{\sigma}^{\mathrm{s}} + \boldsymbol{f}^{\mathrm{s}} \quad \text{in } \Omega^{\mathrm{s}}. \tag{9}$$

The fluid and the structural equations are coupled by the continuity of velocity and traction along the fluid–structure interface.

### 2.2. Interface and boundary conditions

Let $\Gamma = \partial\Omega^{\mathrm{f}}(0) \cap \partial\Omega^{\mathrm{s}}$ be the fluid–structure interface at $t = 0$. Occasionally, we also need $\Gamma(t) = \boldsymbol{\varphi}^{\mathrm{s}}(\Gamma, t)$, which is the fluid–structure interface at time $t$. On $\Gamma$, the FSI system satisfy both velocity and traction continuities

$$\boldsymbol{u}^{\mathrm{f}}\big(\boldsymbol{\varphi}^{\mathrm{s}}(\boldsymbol{z}, t), t\big) = \boldsymbol{u}^{\mathrm{s}}(\boldsymbol{z}, t) \quad \forall \boldsymbol{z} \in \Gamma, \tag{10}$$

$$\int_{\boldsymbol{\varphi}^{\mathrm{s}}(\gamma, t)}\boldsymbol{\sigma}^{\mathrm{f}}(\boldsymbol{x}, t)\mathbf{n}^{\mathrm{f}}da(\boldsymbol{x}) + \int_{\gamma}\boldsymbol{\sigma}^{\mathrm{s}}(\boldsymbol{z}, t)\mathbf{n}^{\mathrm{s}}da(\boldsymbol{z}) = 0 \quad \forall \gamma \subset \Gamma, \tag{11}$$

where $\mathbf{n}^{\mathrm{f}}$ and $\mathbf{n}^{\mathrm{s}}$ are the unit outward normal vectors on $\boldsymbol{\varphi}^{\mathrm{s}}(\gamma, t)$ and $\gamma$, respectively. Here $\gamma$ is any part of $\Gamma$ and $da$ denotes differential surface area. Note that it has been shown in [26, (2.7)] that (11) is equivalent to

$$\left(\det\frac{\partial\boldsymbol{x}}{\partial\boldsymbol{z}}\right)\big(\boldsymbol{\sigma}^{\mathrm{f}}(\boldsymbol{x}(\boldsymbol{z}), t)\big)\left(\frac{\partial\boldsymbol{x}}{\partial\boldsymbol{z}}\right)^{-T}\mathbf{n}^{\mathrm{s}} - \boldsymbol{\sigma}^{\mathrm{s}}(\boldsymbol{z}, t)\mathbf{n}^{\mathrm{s}} = 0, \tag{12}$$

for any $\boldsymbol{z} \in \Gamma$, where $\boldsymbol{x}(\boldsymbol{z}) = \boldsymbol{\varphi}^{\mathrm{s}}(\boldsymbol{z}, t)$. In the literature, the continuity of traction is more often written in the form of (12) (see for example [28, (3)]). But we will use its equivalent form (11) in this paper. Dirichlet and Neumann boundary conditions for the non-interface fluid boundary are given as

$$\boldsymbol{u}^{\mathrm{f}} = \boldsymbol{u}^{\mathrm{f}}_{\mathrm{d}} \quad \text{on } \Sigma_{1} \quad \text{and} \quad \boldsymbol{\sigma}^{\mathrm{f}}\mathbf{n}^{\mathrm{f}} = \boldsymbol{\sigma}^{\mathrm{f}}_{\mathrm{n}} \quad \text{on } \Sigma_{2}, \tag{13}$$

respectively. $\Sigma_1$ and $\Sigma_2$ represent the non-interface Dirichlet and Neumann boundaries of the fluid domain, respectively. $\boldsymbol{u}_d^f$ and $\boldsymbol{\sigma}_n^f$ are specified velocity and traction force on these boundaries, respectively.

Similarly for solid, the boundary conditions on the non-interface boundaries are represented as,

$$\boldsymbol{\varphi}^s = \boldsymbol{\varphi}_d^s \quad \text{on } \Sigma_3 \quad \text{and} \quad \boldsymbol{\sigma}^s \mathbf{n}^s = \boldsymbol{\sigma}_n^s \quad \text{on } \Sigma_4, \tag{14}$$

where $\Sigma_3$ and $\Sigma_4$ represent the non-interface Dirichlet and Neumann boundaries of the solid domain, respectively. Besides the boundary conditions defined in (10)–(14), the governing equations (1), (2) and (4) need to be accompanied with the initial conditions to make the problem well-posed. The initial condition for the fluid velocity is

$$\boldsymbol{u}^f(\cdot, 0) = \boldsymbol{u}_0^f \quad \text{in } \Omega^f(0), \tag{15}$$

where $\boldsymbol{u}_0^f$ is divergence-free. The initial velocity and displacement for the structural dynamics equation (4) are

$$\boldsymbol{u}^s(\cdot, 0) = \boldsymbol{u}_0^s \quad \text{and} \quad \boldsymbol{\varphi}^s(\cdot, 0) = \boldsymbol{\varphi}_0^s \quad \text{in } \Omega^s. \tag{16}$$

Note that $\boldsymbol{u}^f$ and $\boldsymbol{u}^s$ are defined on disparate domains, where $\Omega^s$ is given at the initial time and will never change and $\Omega^f(t)$ varies with respect to $t$. The following subsection describes the weak form of the CFEI formulation.

### 2.3. Weak form of combined field

In order to introduce the weak form of the combined field formulation, let us introduce the trial function space $\mathcal{S}$ along with their corresponding test function space $\mathcal{V}$. The trial function space is defined as

$$\begin{aligned}
\mathcal{S}(\boldsymbol{\varphi}^s, t) = \{ &(\boldsymbol{u}^f, p^f, \boldsymbol{u}^s) | (\boldsymbol{u}^f, p^f, \boldsymbol{u}^s) \in H^1(\Omega^f(t)) \times L^2(\Omega^f(t)) \times H^1(\Omega^s), \\
&\boldsymbol{u}^f(\boldsymbol{\varphi}^s(\boldsymbol{z}, t), t) = \boldsymbol{u}^s(\boldsymbol{z}, t) \; \forall \boldsymbol{z} \in \Gamma, \\
&\boldsymbol{u}^f = \boldsymbol{u}_d^f \text{ on } \Sigma_1 \text{ and } \boldsymbol{u}^s = \partial_t \boldsymbol{\varphi}_d^s \text{ on } \Sigma_3 \},
\end{aligned} \tag{17}$$

The trial function spaces and the corresponding test function spaces differ only at the Dirichlet boundary. The test function spaces are defined as

$$\begin{aligned}
\mathcal{V}(\boldsymbol{\varphi}^s, t) = \{ &(\boldsymbol{\phi}^f, q^f, \boldsymbol{\phi}^s) | (\boldsymbol{\phi}^f, q^f, \boldsymbol{\phi}^s) \in H^1(\Omega^f(t)) \times L^2(\Omega^f(t)) \times H^1(\Omega^s), \\
&\boldsymbol{\phi}^f(\boldsymbol{\varphi}^s(\boldsymbol{z}, t)) = \boldsymbol{\phi}^s(\boldsymbol{z}) \; \forall \boldsymbol{z} \in \Gamma, \\
&\boldsymbol{\phi}^f = 0 \text{ on } \Sigma_1 \text{ and } \boldsymbol{\phi}^s = 0 \text{ on } \Sigma_3 \},
\end{aligned} \tag{18}$$

One may observe that the fluid and structural velocities, and their test functions, respectively, are defined on different domains $\Omega^f(t)$ and $\Omega^s$, and satisfy the matching condition along the interface

$$\boldsymbol{\phi}^f(\boldsymbol{x}) = \boldsymbol{\phi}^s(\boldsymbol{z}) \quad \forall \boldsymbol{z} \in \Gamma, \tag{19}$$

where $\boldsymbol{x} = \boldsymbol{\varphi}^s(\boldsymbol{z}, t)$ with $\boldsymbol{\varphi}^s$ being the position vector of the deformed solid. The weak form of the Navier–Stokes equations (1) and (2) can be written as

$$\int_{\Omega^f(t)} \rho^f(\partial_t \boldsymbol{u}^f + \boldsymbol{u}^f \cdot \nabla \boldsymbol{u}^f) \cdot \boldsymbol{\phi}^f d\boldsymbol{x} + \int_{\Omega^f(t)} \boldsymbol{\sigma}^f : \nabla \boldsymbol{\phi}^f d\boldsymbol{x} = \int_{\Omega^f(t)} \rho^f \boldsymbol{g}^f \cdot \boldsymbol{\phi}^f d\boldsymbol{x} + \int_{\Sigma_2} \boldsymbol{\sigma}_n^f \cdot \boldsymbol{\phi}^f da(\boldsymbol{x}) + \int_{\Gamma(t)} (\boldsymbol{\sigma}^f \mathbf{n}^f) \cdot \boldsymbol{\phi}^f da(\boldsymbol{x}), \tag{20}$$

$$\int_{\Omega^f(t)} \nabla \cdot \boldsymbol{u}^f q^f d\boldsymbol{x} = 0. \tag{21}$$

The weak forms presented in (20) and (21) are obtained by multiplying (1) with $\boldsymbol{\phi}^f$ and (2) with $q^f$ using a dot product, then integrating them over the fluid domain $\Omega^f(t)$. Similarly, we define the weak form of (9) as

$$\int_{\Omega^s} \rho^s \partial_t \boldsymbol{u}^s \cdot \boldsymbol{\phi}^s d\boldsymbol{z} + \int_{\Omega^s} \boldsymbol{\sigma}^s : \nabla \boldsymbol{\phi}^s d\boldsymbol{z} = \int_{\Omega^s} \rho^s \boldsymbol{g}^s \cdot \boldsymbol{\phi}^s d\boldsymbol{z} + \int_{\Sigma_4} \boldsymbol{\sigma}_n^s \cdot \boldsymbol{\phi}^f da(\boldsymbol{z}) + \int_{\Gamma} (\boldsymbol{\sigma}^s \mathbf{n}^s) \cdot \boldsymbol{\phi}^s(\boldsymbol{z}) da(\boldsymbol{z}). \tag{22}$$

Recall the following weak form of the traction continuity condition (11) (see [26, Lemma 2.1])

$$\int_{\boldsymbol{\varphi}^s(\Gamma, t)} (\boldsymbol{\sigma}^f(\boldsymbol{x}, t) \mathbf{n}^f) \cdot \boldsymbol{\phi}^f(\boldsymbol{x}) da(\boldsymbol{x}) + \int_{\Gamma} (\boldsymbol{\sigma}^s(\boldsymbol{z}, t) \mathbf{n}^s) \cdot \boldsymbol{\phi}^s(\boldsymbol{z}) da(\boldsymbol{z}) = 0, \tag{23}$$

where $\boldsymbol{\phi}^f$ and $\boldsymbol{\phi}^s$ are required to satisfy $\boldsymbol{\phi}^f(\boldsymbol{\varphi}^s(\cdot, t)) = \boldsymbol{\phi}^s(\cdot)$ on $\Gamma$. The weak form of the CFEI formulation is achieved by using (23) to combine (20), (21), and (22). Therefore, the weak form of the CFEI formulation is written as, find $(\boldsymbol{u}^f, p^f, \boldsymbol{u}^s) \in \mathcal{S}$ such that for all $(\boldsymbol{\phi}^f, q^f, \boldsymbol{\phi}^s) \in \mathcal{V}$

$$
\int_{\Omega^f(t)} \rho^f (\partial_t \boldsymbol{u}^f + \boldsymbol{u}^f \cdot \nabla \boldsymbol{u}^f) \cdot \boldsymbol{\phi}^f d\boldsymbol{x} + \int_{\Omega^f(t)} \boldsymbol{\sigma}^f : \nabla \boldsymbol{\phi}^f d\boldsymbol{x} - \int_{\Omega^f(t)} \nabla \cdot \boldsymbol{u}^f q^f d\boldsymbol{x} + \int_{\Omega^s} \rho^s \partial_t \boldsymbol{u}^s \cdot \boldsymbol{\phi}^s d\boldsymbol{z} + \int_{\Omega^s} \boldsymbol{\sigma}^s : \nabla \boldsymbol{\phi}^s d\boldsymbol{z}
$$
$$
= \int_{\Omega^f(t)} \rho^f \boldsymbol{g}^f \cdot \boldsymbol{\phi}^f d\boldsymbol{x} + \int_{\Sigma_2} \boldsymbol{\sigma}_n^f \cdot \boldsymbol{\phi}^f da(\boldsymbol{x}) + \int_{\Omega^s} \rho^s \boldsymbol{g}^s \cdot \boldsymbol{\phi}^s d\boldsymbol{z} + \int_{\Sigma_4} \boldsymbol{\sigma}_n^s \cdot \boldsymbol{\phi}^s da(\boldsymbol{z}). \tag{24}
$$

In the CFEI formulation, the velocity continuity condition is enforced in the function space while the Neumann traction continuity condition is built into the weak formulation. During discretization of the coupled system, the two conditions are enforced simultaneously.

### 2.4. ALE formulation and spatial discretization

Given any $t^n \in \mathbb{R}$, when the time $t$ reaches $t^n$, we define a backward in time mapping $\boldsymbol{\Phi}^n(\cdot, t)$ which maps $\Omega^f(t^n)$ to $\Omega^f(t)$ for $t \leq t^n$, and reduces to identity map when $t = t^n$. We can rewrite (24) by non-conservative ALE description,

$$
\int_{\Omega^f(t^n)} \rho^f \left( \frac{d}{dt} \boldsymbol{u}^f (\boldsymbol{\Phi}^n(\boldsymbol{x}, t), t) \Big|_{t=t^n} + (\boldsymbol{u}^f - \partial_t \boldsymbol{\Phi}^n(\boldsymbol{x}, t^n)) \cdot \nabla \boldsymbol{u}^f \right) \cdot \boldsymbol{\phi}^f d\boldsymbol{x}
$$
$$
+ \int_{\Omega^f(t^n)} \boldsymbol{\sigma}^f : \nabla \boldsymbol{\phi}^f d\boldsymbol{x} - \int_{\Omega^f(t)} \nabla \cdot \boldsymbol{u}^f q d\boldsymbol{x} + \int_{\Omega^s} \rho^s \partial_t \boldsymbol{u}^s(\boldsymbol{z}, t^n) \cdot \boldsymbol{\phi}^s d\boldsymbol{z} + \int_{\Omega^s} \boldsymbol{\sigma}^s : \nabla \boldsymbol{\phi}^s d\boldsymbol{z}
$$
$$
= \int_{\Omega^f(t^n)} \rho^f \boldsymbol{g}^f \cdot \boldsymbol{\phi}^f d\boldsymbol{x} + \int_{\Sigma_2} \boldsymbol{\sigma}_n^f \cdot \boldsymbol{\phi}^f da(\boldsymbol{x}) + \int_{\Omega^s} \rho^s \boldsymbol{g}^s \cdot \boldsymbol{\phi}^s d\boldsymbol{z} + \int_{\Sigma_4} \boldsymbol{\sigma}_n^s \cdot \boldsymbol{\phi}^s da(\boldsymbol{z}). \tag{25}
$$

The motion of the spatial coordinates on the fluid domain can be simply modeled as an elastic material in equilibrium,

$$
\nabla \cdot \boldsymbol{\sigma}^m = \boldsymbol{0}, \quad \text{with } \boldsymbol{\sigma}^m = (1 + \tau_m) \big[ (\nabla \boldsymbol{\eta}^f + (\nabla \boldsymbol{\eta}^f)^T) + (\nabla \cdot \boldsymbol{\eta}^f) \boldsymbol{I} \big], \tag{26}
$$

which is deforming under strain introduced by the deformation of the interface subject to the following conditions:

$$
\boldsymbol{\eta}^f = \boldsymbol{\varphi}(\boldsymbol{z}, t) - \boldsymbol{z} \quad \text{on } \Gamma, \qquad \boldsymbol{\eta}^f = 0 \quad \text{on } (\partial \Omega_0^f) \backslash \Gamma \tag{27}
$$

The boundary conditions correspond to the displacement of the fluid–structure interface boundary $\Gamma$. Here $\boldsymbol{\sigma}^m$ is the stress experienced by the fluid mesh, $\boldsymbol{\eta}^f$ is the displacement vector of fluid spatial coordinates $\boldsymbol{x}$ and $\tau_m$ is a local stiffness parameter. In the our discrete scheme, we use $\Omega_{h,t^n}^f$ and $\mathcal{T}_{h,t^n}^f$ to denote the fluid domain and its finite element mesh at $t^n$, respectively. On each triangle $\mathcal{T}_j \in \Omega_{h,0}^f$, $\tau_m = \frac{\max_i |\mathcal{T}_i| - \min_i |\mathcal{T}_i|}{|\mathcal{T}_j|}$ is defined to limit the distortion of the small elements [29]. The result provides position of vertices of all the elements of the fluid mesh $\mathcal{T}_{h,t^n}^f$.

## 3. Second order CFEI scheme

We now turn to the discrete scheme. The scheme is based on an explicit interface advancing which implies that the fluid–structure interface at current time $t^n$ is constructed explicitly using information of the solid at $t^{n-1}$ and $t^{n-2}$. In this way, evaluation of the fluid–structure interface and computations of fluid–structure variables $(\boldsymbol{u}^f, p^f, \boldsymbol{u}^s)$ are decoupled.

In contrast to many FSI schemes available in the literature, e.g. Refs. [30], which apply a finite-volume discretization for the fluid equations in combination with a finite-element discretization for the structural equations, a spatial discretization with finite elements is applied throughout. We adopt the discretization of the weak formulation of CFEI using Galerkin finite element technique. Without the loss of generality, we approximate the fluid velocity, pressure and structural velocity using $\mathbb{P}_m / \mathbb{P}_{m-1} / \mathbb{P}_m$ isoparametric elements to satisfy the inf–sup condition required for the discrete saddle point problem. $\mathcal{T}_{h,t^n}^f$ and $\mathcal{T}_h^s$ represent the triangular mesh on the triangulated domains $\Omega_{h,t^n}^f$ and $\Omega_h^s$, respectively. For efficiency and to achieve optimal approximation property, all edges of internal triangles are taken to be straight.

### 3.1. Temporal discretization

Let $\mathbb{P}_m(\Omega_h)$ denotes the standard $m$th order Lagrange finite element space on domain $\Omega_h$. We employ second order extrapolation to describe the spatial position $\boldsymbol{\varphi}_h^{s,n}$ of the structural domain $\Omega^s$ as

$$\boldsymbol{\varphi}_h^{s,n} = \boldsymbol{\varphi}_h^{s,n-1} + \frac{3\Delta t}{2}\boldsymbol{u}_h^{s,n-1} - \frac{\Delta t}{2}\boldsymbol{u}_h^{s,n-2}. \tag{28}$$

We then use the $\boldsymbol{\varphi}_h^{s,n}(\boldsymbol{z})$ to update the location of the grid points on the fluid structure interface. Next we solve (26) which enables us to determine all the grid points for the $\mathbb{P}_m$ mesh of $\Omega_{h,t^n}^f$, denoted by $\boldsymbol{a}_i^n$ ($i = 1, ..., G$), where $G$ is the total number of grid points. Then we define $\boldsymbol{\Phi}_h^n(\cdot, t^{n-j})$ by

$$\boldsymbol{\Phi}_h^n(\boldsymbol{x}, t) = \sum_{i=1}^{G} \phi_i^{f,n}(\boldsymbol{x})\left[\frac{(t^{n-1}-t)(t^{n-2}-t)}{2\Delta t^2}\boldsymbol{a}_i^n - \frac{(t^n-t)(t^{n-2}-t)}{\Delta t^2}\boldsymbol{a}_i^{n-1} + \frac{(t^n-t)(t^{n-1}-t)}{2\Delta t^2}\boldsymbol{a}_i^{n-2}\right]. \tag{29}$$

Here $\phi_i^{f,n}$ is the scalar $\mathbb{P}_m$ finite element basis function on $\Omega_{h,t^n}^f$ associated with $\boldsymbol{a}_i^n$. It is easy to verify that $\boldsymbol{\Phi}_h^n(\cdot, t^{n-j})$ maps $\Omega_{h,t^n}^f$ to $\Omega_h^f, t^{n-j}$ for $j = 0, 1, 2$, and reduces to an identity map for $j = 0$. We emphasize that the explicit construction $\boldsymbol{\Phi}_h^n$ is not required in the code. It is purely conceptual and has been used to present the scheme (see for example [12, Section 4.4]).

Define $\mathbb{P}_m/\mathbb{P}_{m-1}/\mathbb{P}_m$ solution space $\mathcal{V}_h$ as follows:

$$\mathcal{V}_h(t^n, \boldsymbol{\varphi}_h^{s,n}, \alpha, \boldsymbol{b}) = \{(\boldsymbol{u}_h^f, p_h^f, \boldsymbol{u}_h^s) : \boldsymbol{u}_h^f \in \mathbb{P}_m(\Omega_{h,t^n}^f), p_h^f \in \mathbb{P}_{m-1}(\Omega_{h,t^n}^f), \boldsymbol{u}_h^s \in \mathbb{P}_m(\Omega_h^s),$$
$$\forall \text{ grid point } \boldsymbol{z}_i \text{ of } \mathcal{T}_h^\Gamma, \ \boldsymbol{u}_h^f(\boldsymbol{\varphi}_h^{s,n}(\boldsymbol{z}_i)) = \alpha\boldsymbol{u}_h^{s,n}(\boldsymbol{z}_i) + \boldsymbol{b}\}. \tag{30}$$

Here $\mathcal{T}_h^\Gamma$ represents the finite element mesh along the fluid–structure interface $\Gamma$. The test function space is chosen to be $\mathcal{V}_h(t^n, \boldsymbol{\varphi}_h^{s,n}, 1, \boldsymbol{0})$. There are two parameters $\alpha$ and $\boldsymbol{b}$ in the definition (30). By setting $\alpha = \frac{3}{4}$ and $\boldsymbol{b} = \frac{1}{2}\boldsymbol{u}_h^{s,n-1} - \frac{1}{4}\boldsymbol{u}_h^{s,n-2}$, and then finding $(\boldsymbol{u}_h^{f,n}, p_h^f, \boldsymbol{u}_h^{s,n}) \in \mathcal{V}_h(t^n, \boldsymbol{\varphi}_h^{s,n}, \alpha, \boldsymbol{b})$, we can enforce the following condition on fluid–structure interface

$$\boldsymbol{u}_h^{f,n}(\boldsymbol{\varphi}_h^{s,n}(\boldsymbol{z}_i)) = \frac{3}{4}\boldsymbol{u}_h^{s,n}(\boldsymbol{z}_i) + \frac{1}{2}\boldsymbol{u}_h^{s,n-1}(\boldsymbol{z}_i) - \frac{1}{4}\boldsymbol{u}_h^{s,n-2}(\boldsymbol{z}_i). \tag{31}$$

The above equation is needed for any grid point $\boldsymbol{z}_i$ of $\mathcal{T}_h^\Gamma$. As shown later in Section 4, condition (31) is needed to prove the stability. Fortunately, the accuracy is also maintained since (31) is a second order approximation of the interface condition (10).

Consider the following two functions $\check{\boldsymbol{u}}_h^{f,n}$ and $\boldsymbol{w}_h^n$:

$$\check{\boldsymbol{u}}_h^{f,n}(\boldsymbol{x}) = 2\boldsymbol{u}_h^{f,n-1}(\boldsymbol{\Phi}_h^n(\boldsymbol{x}, t^{n-1})) - \boldsymbol{u}_h^{f,n-2}(\boldsymbol{\Phi}_h^n(\boldsymbol{x}, t^{n-2})), \tag{32}$$

and

$$\boldsymbol{w}_h^n(\boldsymbol{x}) = \sum_{i=1}^{G} \phi_i^{f,n}(\boldsymbol{x})\frac{1}{\Delta t}\left((\boldsymbol{a}_i^n - \boldsymbol{a}_i^{n-1}) + \frac{1}{2}(\boldsymbol{a}_i^{n-1} - \boldsymbol{a}_i^{n-2}) - \frac{1}{2}(\boldsymbol{a}_i^{n-2} - \boldsymbol{a}_i^{n-3})\right)$$
$$= \sum_{i=1}^{G} \phi_i^{f,n}(\boldsymbol{x})\frac{1}{\Delta t}\left(\boldsymbol{a}_i^n - \frac{1}{2}\boldsymbol{a}_i^{n-1} - \boldsymbol{a}_i^{n-2} + \frac{1}{2}\boldsymbol{a}_i^{n-3}\right). \tag{33}$$

Even though $\boldsymbol{w}_h^n(\boldsymbol{x}) \neq \partial_t\boldsymbol{\Phi}_h^n(\boldsymbol{x}, t^n)$ (see (29)), $\boldsymbol{w}_h^n$ is a second order approximation of the fluid mesh velocity $\partial_t\boldsymbol{\Phi}_h^n(\boldsymbol{x}, t^n)$ since

$$f'(t^n) = \frac{1}{\Delta t}\left(f(t^n) - \frac{1}{2}f(t^{n-1}) - f(t^{n-2}) + \frac{1}{2}f(t^{n-3})\right) + O(\Delta t^2).$$

We therefore at least formally will not sacrifice accuracy by using (33). In the present work, we do not directly set $\boldsymbol{w}_h^n(\boldsymbol{x}) = \partial_t\boldsymbol{\Phi}_h^n(\boldsymbol{x}, t^n)$. This ensures the following important result in handling the boundary terms arising from the integration by parts of the nonlinear terms.

**Lemma 1.** Let $\mathcal{T}_{h,t^n}^\Gamma$ be the mesh of the fluid–structure interface $\boldsymbol{\varphi}_h^{s,n}(\Gamma)$ which is part of the boundary of the fluid mesh $\Omega_{h,t^n}^f$, then

$$\boldsymbol{w}_h^n = \check{\boldsymbol{u}}_h^{f,n} \quad \text{on } \mathcal{T}_{h,t^n}^\Gamma. \tag{34}$$

**Proof.** By [12, Proposition 4.3], $\check{\boldsymbol{u}}_h^{f,n} \in \mathbb{P}_m(\Omega_{h,t^n}^f)$ which means it is a finite element function on $\Omega_{h,t^n}^f$. Certainly $\boldsymbol{w}_h^n \in \mathbb{P}_m(\Omega_{h,t^n}^f)$ too. Hence we only need to prove $\boldsymbol{w}_h^n(\boldsymbol{a}_j^n) = \check{\boldsymbol{u}}_h^{f,n}(\boldsymbol{a}_j^n)$ for an arbitrary grid point $\boldsymbol{a}_j^n$ on $\Gamma_{h,t^n}$. To prove the previous equation, we invoke

$$w_h^n(a_j^n) = \frac{1}{\Delta t}\left((a_j^n - a_j^{n-1}) + \frac{1}{2}(a_j^{n-1} - a_j^{n-2}) - \frac{1}{2}(a_j^{n-2} - a_j^{n-3})\right)$$

$$= \frac{\varphi_h^{s,n}(z_j) - \varphi_h^{s,n-1}(z_j)}{\Delta t} + \frac{\varphi_h^{s,n-1}(z_j) - \varphi_h^{s,n-2}(z_j)}{2\Delta t} - \frac{\varphi_h^{s,n-2}(z_j) - \varphi_h^{s,n-3}(z_j)}{2\Delta t},$$

where $z_j$ is a grid point on $\Gamma$ and is the pre-image of $a_j^n \in \Gamma_{h,t^n}$ under the mapping $\varphi_h^{s,n}$.

Now, plugging in the definition of $\varphi_h^{s,n}$ in (28) into the above equation and simplifying, we obtain

$$w_h^n(a_j^n) = 2\left(\frac{3}{4}u_h^{s,n-1}(z_j) + \frac{1}{2}u_h^{s,n-2}(z_j) - \frac{1}{4}u_h^{s,n-3}(z_j)\right)$$

$$- \left(\frac{3}{4}u_h^{s,n-2}(z_j) + \frac{1}{2}u_h^{s,n-3}(z_j) - \frac{1}{4}u_h^{s,n-4}(z_j)\right).$$

With the aid of (31) and the fact that $a_j^n = \varphi_h^{s,n}(z_j)$, we finally obtain $w_h^n(a_j^n) = \check{u}_h^{f,n}(a_j^n)$ from the above equation. □

The above lemma is instrumental to obtain the stability result presented in Section 4. The fully discrete scheme for the second-order CFEI formulation is presented in the next subsection.

### 3.2. Complete scheme

After the above preparations, we are finally ready to solve for the finite element discretized CFEI form. Find

$$\left(u_h^{f,n}, p_h^{f,n}, u_h^{s,n}\right) \in \mathcal{V}_h\left(t^n, \varphi_h^{s,n}, \frac{3}{4}, \frac{1}{2}u_h^{s,n-1} - \frac{1}{4}u_h^{s,n-2}\right) \tag{35}$$

with $u_h^{f,n}|_{\Sigma_1} = u_b^f$ and $u_h^{s,n}|_{\Sigma_3} = \partial_t \varphi_b^s$ so that for any finite element triple

$$\left(\phi^f, q^f, \phi^s\right) \in \mathcal{V}_h\left(t^n, \varphi_h^{s,n}, 1, \mathbf{0}\right) \tag{36}$$

with $\phi_h^f|_{\Sigma_1} = 0$ and $\phi_h^s|_{\Sigma_3} = 0$, such that

$$\left. \begin{aligned} \int_{\Omega_{h,t^n}^f} &\left[\frac{\rho^f}{\Delta t}\left(\frac{3}{2}u_h^{f,n}(x) - 2u_h^{f,n-1}\left(\Phi_h^n(x,t^{n-1})\right) + \frac{1}{2}u_h^{f,n-2}\left(\Phi_h^n(x,t^{n-2})\right)\right) \right. \\ &\left. + \left(\check{u}_h^{f,n} - w_h^n\right)\cdot\nabla u_h^{f,n} + \frac{1}{2}\left(\nabla\cdot\check{u}_h^{f,n}\right)u_h^{f,n}\right]\cdot\phi^f dx \\ &+ \int_{\Omega_{h,t^n}^f} \rho^f \nu^f\left(\nabla u_h^{f,n} + \left(\nabla u_h^{f,n}\right)^T\right):\nabla\phi^f dx \end{aligned}\right\} A$$

$$\left. -\int_{\Omega_{h,t^n}^f} p_h^{f,n}\left(\nabla\cdot\phi^f\right)dx \right\} B$$

$$\left. -\int_{\Omega_{h,t^n}^f} q^f\left(\nabla\cdot u_h^{f,n}\right)dx \right\} C$$

$$\left. \begin{aligned} &+\int_{\Omega_h^s} \frac{\rho^s}{\Delta t}\left(\frac{3}{2}u_h^{s,n} - 2u_h^{s,n-1} + \frac{1}{2}u_h^{s,n-2}\right)\cdot\phi^s dz \\ &+\frac{1}{2}\int_{\Omega_h^s}\left(\sigma^s\left(\varphi_h^{s,n-1}\right) + \sigma^s\left(\varphi_h^{s,n+1}\right)\right):\nabla\phi^s dz \end{aligned}\right\} D$$

$$\left. = \int_{\Omega_{h,t^n}^f} \rho^f g^f\cdot\phi^f dx + \int_{\Sigma_2}\sigma_n^f\cdot\phi^f da(x) + \int_{\Omega_h^s}\rho^f g^s\cdot\phi^s dz + \int_{\Sigma_4}\sigma_n^s\cdot\phi^f da(z), \right\} E \tag{37}$$

where $A$ denotes the transient, convective and diffusive contributions, $B$ and $C$, respectively, are the pressure and continuity terms, $D$ represents the solid momentum equation, while $E$ denotes the body force and boundary conditions. The technique of adding the term $\frac{1}{2}(\nabla \cdot \breve{\boldsymbol{u}}_h^{f,n})\boldsymbol{u}_h^{f,n}$ in part A of (37) is due to [31]. It is by now a standard technique. The idea is to observe that if $b(u, v, w) = (u \cdot \nabla v, w) + \frac{1}{2}((\nabla \cdot u)v, w)$, then $b(u, v, v) = 0$ for any $u$ and $v$ as long as $u \cdot \boldsymbol{n}^f$ or $v$ vanishes on the boundary. So when $\boldsymbol{\phi}^f = \boldsymbol{u}_h^{f,n}$, the second line in part A would becomes $-\frac{1}{2}\boldsymbol{w}_h^n \cdot \nabla |\boldsymbol{u}_h^{f,n}|^2$ and the nonlinear terms drop. Here we have also used (34).

The $\boldsymbol{\varphi}_h^{s,n+1}$ in Part D of (37) has been defined as $\boldsymbol{\varphi}_h^{s,n+1} = \boldsymbol{\varphi}_h^{s,n} + \frac{3\Delta t}{2}\boldsymbol{u}_h^{s,n} - \frac{\Delta t}{2}\boldsymbol{u}_h^{s,n-1}$ (see (28)). For nonlinear elastic material, we can approximate the last term in Part $D$ of (37) as sum of a known forcing term and a linear term for the unknown $\boldsymbol{u}_h^{s,n}$,

$$\int\limits_{\Omega_h^s} \boldsymbol{\sigma}^s \left( \boldsymbol{\varphi}_h^{s,n} - \frac{\Delta t}{2}\boldsymbol{u}_h^{s,n-1} \right) : \nabla \boldsymbol{\phi}^s d\boldsymbol{z} + \frac{3\Delta t}{2}A_s \left( \nabla \left( \boldsymbol{\varphi}_h^{s,n} - \frac{\Delta t}{2}\boldsymbol{u}_h^{s,n-1} \right); \nabla \boldsymbol{u}_h^{s,n}, \nabla \boldsymbol{\phi}^s \right). \tag{38}$$

We have ignored a remainder term of size $O(\Delta t^2)$ in the above linearization. For a St. Venant–Kirchhoff material (see [26, Section 3.1]), the quantity $A_s$ can be written as

$$A_s(\boldsymbol{F}; \boldsymbol{G}, \boldsymbol{H}) = \int\limits_{\Omega^s} \left( \lambda^s (\mathrm{tr}\, \boldsymbol{E})\boldsymbol{H} : \boldsymbol{G} + \frac{\lambda^s}{4} \mathrm{tr}(\boldsymbol{H}^T \boldsymbol{F} + \boldsymbol{F}^T \boldsymbol{H}) \mathrm{tr}(\boldsymbol{G}^T \boldsymbol{F} + \boldsymbol{F}^T \boldsymbol{G}) \right.$$

$$\left. + \mu^s \boldsymbol{E} : (\boldsymbol{H}^T \boldsymbol{G} + \boldsymbol{G}^T \boldsymbol{H}) + \frac{\mu^s}{2} (\boldsymbol{H}^T \boldsymbol{F} + \boldsymbol{F}^T \boldsymbol{H}) : (\boldsymbol{G}^T \boldsymbol{F} + \boldsymbol{F}^T \boldsymbol{G}) \right), \tag{39}$$

where $\boldsymbol{E} = \frac{1}{2}(\boldsymbol{F}\boldsymbol{F}^T - I)$ and $\boldsymbol{H} : \boldsymbol{G} = \mathrm{tr}(\boldsymbol{H}^T \boldsymbol{G})$. $A_s(\boldsymbol{F}; \boldsymbol{G}, \boldsymbol{H})$ is a bilinear functional of $\boldsymbol{G}$ and $\boldsymbol{H}$. Therefore, $\boldsymbol{G}$ and $\boldsymbol{H}$ for (38) will be $\nabla \boldsymbol{u}_h^{s,n}$ and $\nabla \boldsymbol{\phi}^s$, respectively.

### 3.3. Algorithm

The basic steps to be performed in the CFEI scheme are summarized as follows:

---

**Algorithm 1** Second-order scheme for FSI.

---

1. Start from known solutions $\boldsymbol{u}_h^{f,n-1}, \boldsymbol{u}_h^{f,n-2}, \boldsymbol{u}_h^{s,n-1}, \boldsymbol{u}_h^{s,n-2}, \boldsymbol{\varphi}_h^{s,n-1}$ at time $t^{n-1}$
2. Advance from $t^{n-1}$ to $t^n$
   (a) Define the structural position $\boldsymbol{\varphi}_h^{s,n}$ using (28)
   (b) Determine positions of vertices of triangles on the fluid domain $\Omega_{h,t^n}^f$ by solving (26) using $\mathbb{P}_1$ elements on $\Omega_{h,0}^f$
   (c) Use result from (b) to determine the updated mesh of $\Omega_{h,t^n}^f$
   (d) Define $\breve{\boldsymbol{u}}_h^{f,n}$ and $\boldsymbol{w}_h^n$ by (32) and (33)
   (e) Solve the updated field variables $\boldsymbol{u}_h^{f,n}, p_h^{f,n}, \boldsymbol{u}_h^{s,n}$ at current time $t^n$ using (37)

---

At each time step, the present CFEI scheme requires to solve only once for a linearized system of the Navier–Stokes flow interacting with an elastic structure. No Newton–Raphson type iteration is required for this mathematically nonlinear problem. Solving of linear system of equations only once per time step, makes the proposed scheme very efficient. Even though a direct solver has been used in this paper, one can switch to Krylov subspace based iterative solvers when the size of the problem becomes very large.

One may realize that the solutions obtained with the CFEI scheme retains and carries over the linearization errors rather than eliminating them through further iterations. Further iteration may reduce the linearization error with a significant increase in the cost, however, the linearization error is still part of the total numerical error. See for example [12,32,33] for related theoretical and numerical studies on semi-implicit schemes where optimal order of convergence can be attained without resorting to further nonlinear iterations. In this paper, we are more concerned about reducing the total error and hope to find the most economic way to reach the desired order of accuracy. As long as the scheme has the desired order of accuracy, reduction in the total error can be achieved by decreasing temporal $\Delta t$ and spatial $h$ resolutions. By linearization with high-order extrapolation, we keep the order of accuracy to be quadratic in this work.

## 4. Stability and convergence

In this section, we want to prove the stability of second-order CFEI scheme by showing that the solutions of (37) are uniformly bounded for all $n \geq 0$.

### 4.1. Stability settings and requirements

To prove the boundedness of the solid material part, the term D in (37) is considered. Using (28), the temporal term in D can be simplified to

$$\frac{\frac{3}{2}\boldsymbol{u}_h^{s,n} - 2\boldsymbol{u}_h^{s,n-1} + \frac{1}{2}\boldsymbol{u}_h^{s,n-2}}{\Delta t} = \frac{(\boldsymbol{\varphi}_h^{s,n+1} - \boldsymbol{\varphi}_h^{s,n}) - (\boldsymbol{\varphi}_h^{s,n} - \boldsymbol{\varphi}_h^{s,n-1})}{\Delta t^2}.$$

Hence the second-order backward difference formula used in Part D in (37) is the familiar trapezoidal rule for elastodynamics (assuming free vibration for simplicity):

$$\int_{\Omega_h^s} \rho^s \frac{(\boldsymbol{\varphi}_h^{s,n+1} - 2\boldsymbol{\varphi}_h^{s,n} + \boldsymbol{\varphi}_h^{s,n-1})}{\Delta t^2} \cdot \boldsymbol{\phi}^s d\boldsymbol{z} + \frac{1}{2}\int_{\Omega_h^s} \left(\boldsymbol{\sigma}^s(\boldsymbol{\varphi}_h^{s,n-1}) + \boldsymbol{\sigma}^s(\boldsymbol{\varphi}_h^{s,n+1})\right) : \nabla \boldsymbol{\phi}^s d\boldsymbol{z} = 0. \tag{40}$$

To prove its stability, we choose the following approximation

$$\boldsymbol{\phi}^s = \frac{\boldsymbol{\varphi}^{s,n+1} - \boldsymbol{\varphi}^{s,n-1}}{2} \tag{41}$$

From simple algebraic arrangements, we have

$$\boldsymbol{\phi}^s = \frac{(\boldsymbol{\varphi}_h^{s,n+1} - \boldsymbol{\varphi}_h^{s,n}) + (\boldsymbol{\varphi}_h^{s,n} - \boldsymbol{\varphi}_h^{s,n-1})}{2} = \frac{\boldsymbol{\eta}_h^{s,n+1} - \boldsymbol{\eta}_h^{s,n-1}}{2},$$

where $\boldsymbol{\eta}_h^{s,n+1}(\boldsymbol{z}) = \boldsymbol{\varphi}_h^{s,n+1}(\boldsymbol{z}) - \boldsymbol{z}$. For a linear elastic solid (5), we can define

$$\left\|\boldsymbol{\epsilon}(\boldsymbol{\varphi}_h^s)\right\|_s^2 = \int_{\Omega^s} \boldsymbol{\sigma}^s(\boldsymbol{\varphi}_h^s) : \nabla \boldsymbol{\eta}_h^s = \frac{\mu^s}{2}\left\|\nabla \boldsymbol{\eta}_h^s + \left(\nabla \boldsymbol{\eta}_h^s\right)^T\right\|^2 + \lambda^s\left\|\nabla \cdot \boldsymbol{\eta}_h^s\right\|^2.$$

From (40), assuming linear elasticity, we immediately obtain

$$L_n - L_{n-1} = 0, \tag{42}$$

where the energy estimate

$$L_n = \frac{\rho^s}{2\Delta t^2}\int_{\Omega_h^s} \left|\boldsymbol{\varphi}_h^{s,n+1} - \boldsymbol{\varphi}_h^{s,n}\right|^2 d\boldsymbol{z} + \frac{1}{4}\left(\left\|\boldsymbol{\epsilon}(\boldsymbol{\varphi}_h^{s,n+1})\right\|_s^2 + \left\|\boldsymbol{\epsilon}(\boldsymbol{\varphi}_h^{s,n})\right\|_s^2\right).$$

Thus we have the stability for the solid part.

To prove the stability of the fluid part, consider the following identity which gives us a telescope plus a positive term

$$\begin{aligned}\left(\frac{3}{2}u^n - 2u^{n-1} + \frac{1}{2}u^{n-2}\right)u^n &= \frac{1}{4}|u^n|^2 - \frac{1}{4}|u^{n-1}|^2 \\ &\quad + \frac{1}{4}|2u^n - u^{n-1}|^2 - \frac{1}{4}|2u^{n-1} - u^{n-2}|^2 \\ &\quad + \frac{1}{4}|u^n - 2u^{n-1} + u^{n-2}|^2.\end{aligned} \tag{43}$$

Motivated by the above identity, we set

$$\boldsymbol{\phi}^f = \Delta t \boldsymbol{u}_h^{f,n}$$

and $q^f = -p_h^n$, respectively, in (37). These choices, however, must satisfy the compatibility conditions proposed in the requirement $(\boldsymbol{\phi}^f, q^f, \boldsymbol{\phi}^s) \in \mathcal{V}_h(t^n, \boldsymbol{\varphi}_h^{s,n}, 1, \boldsymbol{0})$:

$$\forall \text{ grid point } \boldsymbol{z}_i \text{ of } \mathcal{T}_h^\Gamma, \ \boldsymbol{\phi}^f(\boldsymbol{\varphi}_h^{s,n}(\boldsymbol{z}_i)) = \boldsymbol{\phi}^s(\boldsymbol{z}_i). \tag{44}$$

Using (28), it is easy to verify that $\boldsymbol{\phi}^s$ defined by (41) satisfies

$$\boldsymbol{\phi}^s = \Delta t\left(\frac{3}{4}\boldsymbol{u}_h^{s,n} + \frac{1}{2}\boldsymbol{u}_h^{s,n-1} - \frac{1}{4}\boldsymbol{u}_h^{s,n-2}\right).$$

The condition (44) is satisfied due to the requirement of (35) (see (31)).

From now on, we use the notations

$$\langle\cdot,\cdot\rangle_{(t^j)} = \langle\cdot,\cdot\rangle_{\Omega_{h,t^j}^f}, \qquad \|\cdot\|_{(t^j)} = \langle\cdot,\cdot\rangle_{(t^j)}^{\frac{1}{2}}, \tag{45}$$

$$\int_{\Omega_{h,t^j}^f} g(\boldsymbol{x})d\boldsymbol{x} = \int_{(t^j)} g(\boldsymbol{x})d\boldsymbol{x}. \tag{46}$$

As the energy bound alone at $t^n$ is not sufficient to prevent the fluid–structure interface from colliding with itself or other fixed boundaries at $t^n$, hence we need to assume that $\boldsymbol{\varphi}_h^{s,n}$ obtained by (28) allows us to successfully construct $\Omega_{h,t^n}^f$ using Step 2(b) of the CFEI Algorithm. This confirms that the new mesh is not turned inside out and the local ordering of the vertices of each element is preserved. If $\{\boldsymbol{a}_{i_0}^n, \boldsymbol{a}_{i_1}^n, ..., \boldsymbol{a}_{i_d}^n\}$ denotes $(d+1)$ vertices of the ith element of the mesh of $\Omega_{h,t^n}^f \subset \mathbb{R}^d$, the preservation of local ordering requires

$$\left(\det[\boldsymbol{a}_{i_1}^n - \boldsymbol{a}_{i_0}^n, ..., \boldsymbol{a}_{i_d}^n - \boldsymbol{a}_{i_0}^n]\right)\left(\det[\boldsymbol{a}_{i_1}^0 - \boldsymbol{a}_{i_0}^0, ..., \boldsymbol{a}_{i_d}^0 - \boldsymbol{a}_{i_0}^0]\right) > 0, \quad \forall i. \tag{47}$$

Note that we compare the ordering at time $t^n$ with the one at time $t^0$, and according to Step 2(b) of the Algorithm, the displacement is defined with respect to the reference mesh at $t^0$.

### 4.2. Stability proof

Now we are ready to state the stability result. First, let us introduce

$$M_n = \frac{\rho^f}{4}\left\|\boldsymbol{u}_h^{f,n}\right\|_{(t^n)}^2 + \frac{\rho^f}{4}\left\|2\boldsymbol{u}_h^{f,n} - \boldsymbol{u}_h^{f,n-1}(\boldsymbol{\Phi}_h^n(t^{n-1}))\right\|_{(t^n)}^2$$
$$+ \frac{\rho^s}{8}\left\|3\boldsymbol{u}_h^{s,n} - \boldsymbol{u}_h^{s,n-1}\right\|_s^2 + \frac{1}{4}\left(\left\|\boldsymbol{\epsilon}(\boldsymbol{\varphi}_h^{s,n+1})\right\|_s^2 + \left\|\boldsymbol{\epsilon}(\boldsymbol{\varphi}_h^{s,n})\right\|_s^2\right). \tag{48}$$

and define

$$C^n = \frac{(\max|\det(\partial \boldsymbol{x}^n/\partial \boldsymbol{x}^{n-1})|) - 1}{\Delta t}, \qquad D^n = \rho^s \max(\nabla \cdot \boldsymbol{w}_h^n), \tag{49}$$

where $\boldsymbol{x}^n : \boldsymbol{x}^{n-1} \mapsto \boldsymbol{x}^n$ is the inverse of the mapping $\boldsymbol{\Phi}_h^n(\cdot, t^{n-1}) : \boldsymbol{x}^n \mapsto \boldsymbol{x}^{n-1}$. Here the maximums in $C^n$ or $D^n$ are taken piecewisely and run through all the triangles in $\Omega_{h,t^{n-1}}^f$ or $\Omega_{h,t^n}^f$, respectively. Note that $C^n$ and $D^n$ vanish if the fluid domain does not move. $C^n$ and $D^n$ are of size $O(1)$ if the fluid domain moves with finite speed.

**Theorem 1.** *Assume linear elasticity (5). Assume $\boldsymbol{u}_d^f = 0$, $\Sigma_2 = \emptyset$, $\partial_t \boldsymbol{\varphi}_d^s = 0$, and $\boldsymbol{\sigma}_n^s = 0$. If $\boldsymbol{\varphi}_h^{s,n}$ ensures (47),*

$$M_n - M_{n-1} + \rho^f \nu^f \Delta t\left\|\boldsymbol{\epsilon}^f(\boldsymbol{u}_h^{f,n})\right\|_{(t^n)}^2 \leq (C^n + 1)\Delta t M_{n-1} + (2D^n + 1)\Delta t M_n$$
$$+ \Delta t K\left(\rho^f\left\|\boldsymbol{g}^f\right\|_{(t^n)}^2 + \rho^s\left\|\boldsymbol{g}^s\right\|_s^2\right) \tag{50}$$

*for some universal constant $K$. If $C^n$ and $D^n$ are uniformly bounded in terms of $n$, which means that the fluid mesh moves with a velocity whose size is uniformly bounded, (50) implies stability by the discrete Gronwall inequality ([34, Lemma 1.4.2] [12, Lemma 5.3]).*

**Proof.** Let us set $\boldsymbol{\phi}^f = \Delta t \boldsymbol{u}_h^{f,n}$ in (37) and examine the second line in Part A:

$$\Delta t \int\limits_{(t^n)} \left((\check{\boldsymbol{u}}_h^{f,n} - \boldsymbol{w}_h^n) \cdot \nabla \boldsymbol{u}_h^{f,n} + \frac{1}{2}(\nabla \cdot \check{\boldsymbol{u}}_h^{f,n})\boldsymbol{u}_h^{f,n}\right) \cdot \boldsymbol{u}_h^{f,n}d\boldsymbol{x}$$
$$= \Delta t \int\limits_{(t^n)} -\nabla \cdot (\check{\boldsymbol{u}}_h^{f,n} - \boldsymbol{w}_h^n)\frac{1}{2}|\boldsymbol{u}_h^{f,n}|^2 + \frac{1}{2}(\nabla \cdot \check{\boldsymbol{u}}_h^{f,n})|\boldsymbol{u}_h^{f,n}|^2 d\boldsymbol{x}$$
$$= \frac{\Delta t}{2} \int\limits_{(t^n)} \nabla \cdot \boldsymbol{w}_h^n |\boldsymbol{u}_h^{f,n}|^2 d\boldsymbol{x}. \tag{51}$$

In the second step, we have used the integration by parts for the first term. We do not pick up a boundary term in this step because of (34). The vanishing of the boundary term is crucial for the stability proof since otherwise we have no control on this integral in the proof.

In (37), let $\boldsymbol{\phi}^f = \Delta t \boldsymbol{u}_h^{f,n}$, $q^f = -p_h^{f,n}$ and $\boldsymbol{\phi}^s = \Delta t(\frac{3}{4}\boldsymbol{u}_h^{s,n} + \frac{1}{2}\boldsymbol{u}_h^{s,n-1} - \frac{1}{4}\boldsymbol{u}_h^{s,n-2})$. Denote $\frac{3}{4}\boldsymbol{u}_h^{s,n} + \frac{1}{2}\boldsymbol{u}_h^{s,n-1} - \frac{1}{4}\boldsymbol{u}_h^{s,n-2}$ by $\tilde{\boldsymbol{u}}_h^{s,n}$. Because of (42), (43) and (51), (37) leads to

$$\frac{\rho^f}{4}\left\|\boldsymbol{u}_h^{f,n}\right\|_{(t^n)}^2 - \frac{\rho^f}{4}\left\|\boldsymbol{u}_h^{f,n-1}(\boldsymbol{\Phi}_h^n(t^{n-1}))\right\|_{(t^n)}^2$$
$$+ \frac{\rho^f}{4}\left\|2\boldsymbol{u}_h^{f,n} - \boldsymbol{u}_h^{f,n-1}(\boldsymbol{\Phi}_h^n(t^{n-1}))\right\|_{(t^n)}^2 - \frac{\rho^f}{4}\left\|2\boldsymbol{u}_h^{f,n-1}(\boldsymbol{\Phi}_h^n(t^{n-1})) - \boldsymbol{u}_h^{f,n-2}(\boldsymbol{\Phi}_h^n(t^{n-2}))\right\|_{(t^n)}^2$$

$$+ \frac{\rho^{\mathrm{f}}\Delta t}{2} \int\limits_{(t^{\mathrm{n}})} \left(\nabla \cdot \boldsymbol{w}_{\mathrm{h}}^{\mathrm{n}}\right) |\boldsymbol{u}_{\mathrm{h}}^{\mathrm{f},\mathrm{n}}|^2 d\boldsymbol{x} + \frac{\rho^{\mathrm{f}}\nu^{\mathrm{f}}\Delta t}{2} \left\|\nabla \boldsymbol{u}_{\mathrm{h}}^{\mathrm{f},\mathrm{n}} + \left(\nabla \boldsymbol{u}_{\mathrm{h}}^{\mathrm{f},\mathrm{n}}\right)^T\right\|_{(t^{\mathrm{n}})}^2$$

$$+ \frac{\rho^{\mathrm{s}}}{8} \left\|3\boldsymbol{u}_{\mathrm{h}}^{\mathrm{s},\mathrm{n}} - \boldsymbol{u}_{\mathrm{h}}^{\mathrm{s},\mathrm{n}-1}\right\|_s^2 - \frac{\rho^{\mathrm{s}}}{8} \left\|3\boldsymbol{u}_{\mathrm{h}}^{\mathrm{s},\mathrm{n}-1} - \boldsymbol{u}_{\mathrm{h}}^{\mathrm{s},\mathrm{n}-2}\right\|_s^2 + \frac{1}{4} \left\|\boldsymbol{\epsilon}\left(\boldsymbol{\varphi}_{\mathrm{h}}^{\mathrm{s},\mathrm{n}+1}\right)\right\|_s^2 - \frac{1}{4} \left\|\boldsymbol{\epsilon}\left(\boldsymbol{\varphi}_{\mathrm{h}}^{\mathrm{s},\mathrm{n}-1}\right)\right\|_s^2$$

$$\leq \Delta t \langle \rho^{\mathrm{f}}\boldsymbol{g}^{\mathrm{f}}, \boldsymbol{u}_{\mathrm{h}}^{\mathrm{f},\mathrm{n}}\rangle_{(t^{\mathrm{n}})} + \Delta t \langle \rho^{\mathrm{s}}\boldsymbol{g}^{\mathrm{s}}, \tilde{\boldsymbol{u}}_{\mathrm{h}}^{\mathrm{s},\mathrm{n}}\rangle_{\Omega^s}. \tag{52}$$

Note that

$$\int\limits_{(t^{\mathrm{n}})} \left|\boldsymbol{u}_{\mathrm{h}}^{\mathrm{f},\mathrm{n}-1}\left(\Phi_{\mathrm{h}}^{\mathrm{n}}\left(\boldsymbol{x}^{\mathrm{n}}, t^{\mathrm{n}-1}\right)\right)\right|^2 d\boldsymbol{x}^{\mathrm{n}} = \int\limits_{(t^{\mathrm{n}-1})} \left|\boldsymbol{u}_{\mathrm{h}}^{\mathrm{f},\mathrm{n}-1}\left(\boldsymbol{x}^{\mathrm{n}-1}\right)\right|^2 \left|\det \frac{\partial \boldsymbol{x}^{\mathrm{n}}}{\partial \boldsymbol{x}^{\mathrm{n}-1}}\right| d\boldsymbol{x}^{\mathrm{n}-1}.$$

Hence

$$\left\|\boldsymbol{u}_{\mathrm{h}}^{\mathrm{f},\mathrm{n}-1}\left(\Phi_{\mathrm{h}}^{\mathrm{n}}\left(\cdot, t^{\mathrm{n}-1}\right)\right)\right\|_{(t^{\mathrm{n}})}^2 \leq \left(1 + C^{\mathrm{n}}\Delta t\right) \left\|\boldsymbol{u}_{\mathrm{h}}^{\mathrm{f},\mathrm{n}-1}\right\|_{(t^{\mathrm{n}-1})}^2.$$

Similarly (see [12, Lemma 5.1]),

$$\left\|2\boldsymbol{u}_{\mathrm{h}}^{\mathrm{f},\mathrm{n}-1}\left(\Phi_{\mathrm{h}}^{\mathrm{n}}\left(\cdot, t^{\mathrm{n}-1}\right)\right) - \boldsymbol{u}_{\mathrm{h}}^{\mathrm{f},\mathrm{n}-2}\left(\Phi_{\mathrm{h}}^{\mathrm{n}}\left(\cdot, t^{\mathrm{n}-2}\right)\right)\right\|_{(t^{\mathrm{n}})}^2 \leq \left(1 + C^{\mathrm{n}}\Delta t\right) \left\|2\boldsymbol{u}_{\mathrm{h}}^{\mathrm{f},\mathrm{n}-1}(\cdot) - \boldsymbol{u}_{\mathrm{h}}^{\mathrm{f},\mathrm{n}-2}\left(\Phi_{\mathrm{h}}^{\mathrm{n}-1}\left(\cdot, t^{\mathrm{n}-2}\right)\right)\right\|_{(t^{\mathrm{n}-1})}^2.$$

Applying the last two inequalities in (52), we obtain

$$M_{\mathrm{n}} - M_{\mathrm{n}-1} + 2\rho^{\mathrm{f}}\nu^{\mathrm{f}}\Delta t \left\|\boldsymbol{\epsilon}^{\mathrm{f}}\left(\boldsymbol{u}_{\mathrm{h}}^{\mathrm{f},\mathrm{n}}\right)\right\|_{(t^{\mathrm{n}})}^2 \leq \frac{1}{4} C^{\mathrm{n}}\Delta t \left(\left\|\boldsymbol{u}_{\mathrm{h}}^{\mathrm{f},\mathrm{n}-1}\right\|_{(t^{\mathrm{n}-1})}^2 + \left\|2\boldsymbol{u}_{\mathrm{h}}^{\mathrm{f},\mathrm{n}-1} - \boldsymbol{u}_{\mathrm{h}}^{\mathrm{f},\mathrm{n}-2}\left(\Phi_{\mathrm{h}}^{\mathrm{n}-1}\left(\cdot, t^{\mathrm{n}-2}\right)\right)\right\|_{(t^{\mathrm{n}-1})}^2\right)$$

$$+ \frac{1}{2} D^{\mathrm{n}}\Delta t \left\|\boldsymbol{u}_{\mathrm{h}}^{\mathrm{f},\mathrm{n}}\right\|_{(t^{\mathrm{n}})}^2 + \Delta t \langle \rho^{\mathrm{f}}\boldsymbol{g}^{\mathrm{f}}, \boldsymbol{u}_{\mathrm{h}}^{\mathrm{f},\mathrm{n}}\rangle_{(t^{\mathrm{n}})} + \Delta t \langle \rho^{\mathrm{s}}\boldsymbol{g}^{\mathrm{s}}, \tilde{\boldsymbol{u}}_{\mathrm{h}}^{\mathrm{s},\mathrm{n}}\rangle_{\Omega^s}$$

$$\leq C^{\mathrm{n}}\Delta t M_{\mathrm{n}-1} + 2D^{\mathrm{n}}\Delta t M_{\mathrm{n}} + \Delta t \langle \rho^{\mathrm{f}}\boldsymbol{g}^{\mathrm{f}}, \boldsymbol{u}_{\mathrm{h}}^{\mathrm{f},\mathrm{n}}\rangle_{(t^{\mathrm{n}})} + \Delta t \langle \rho^{\mathrm{s}}\boldsymbol{g}^{\mathrm{s}}, \tilde{\boldsymbol{u}}_{\mathrm{h}}^{\mathrm{s},\mathrm{n}}\rangle_{\Omega^s}. \tag{53}$$

Note that (i) Korn's inequality [35] says that

$$\left\|\boldsymbol{u}_{\mathrm{h}}^{\mathrm{f},\mathrm{n}}\right\|_{(t^{\mathrm{n}})} \leq C \left\|\boldsymbol{\epsilon}^{\mathrm{f}}\left(\boldsymbol{u}_{\mathrm{h}}^{\mathrm{f},\mathrm{n}}\right)\right\|_{(t^{\mathrm{n}})}$$

for some universal constant $C$; (ii) the definition of $\tilde{\boldsymbol{u}}_{\mathrm{h}}^{\mathrm{s},\mathrm{n}}$ implies

$$\rho^{\mathrm{s}} \left\|\tilde{\boldsymbol{u}}_{\mathrm{h}}^{\mathrm{s},\mathrm{n}}\right\|_s^2 \leq \frac{\rho^{\mathrm{s}}}{8} \left\|3\boldsymbol{u}_{\mathrm{h}}^{\mathrm{s},\mathrm{n}} - \boldsymbol{u}_{\mathrm{h}}^{\mathrm{s},\mathrm{n}-1}\right\|_s^2 + \frac{\rho^{\mathrm{s}}}{8} \left\|3\boldsymbol{u}_{\mathrm{h}}^{\mathrm{s},\mathrm{n}-1} - \boldsymbol{u}_{\mathrm{h}}^{\mathrm{s},\mathrm{n}-2}\right\|_s^2 \leq M_{\mathrm{n}} + M_{\mathrm{n}-1}.$$

Hence we derive (50) by using the following Cauchy–Schwartz inequality to the last two body forcing terms in (53):

$$\left|\int\limits_{\Omega} fg\right| \leq \left(\int\limits_{\Omega} |f|^2\right)^{1/2} \left(\int\limits_{\Omega} |g|^2\right)^{1/2} \leq c\left(\int\limits_{\Omega} |f|^2\right) + \frac{1}{4c}\left(\int\limits_{\Omega} |g|^2\right) \quad \forall c > 0.$$

This completes the proof of (50). $\quad\square$

**Remark 1.** Even though the boundness of $M_{\mathrm{n}}$ cannot guarantee an inequality like (47) with n replaced by $\mathrm{n}+1$, it does guarantee the boundness of $\|\boldsymbol{\epsilon}(\boldsymbol{\varphi}_{\mathrm{h}}^{\mathrm{s},\mathrm{n}+1})\|_s^2$, refer (48) for the definition of $M_{\mathrm{n}}$. One may remember that, we precisely use $\boldsymbol{\varphi}_{\mathrm{h}}^{\mathrm{s},\mathrm{n}+1}$ to construct the fluid mesh at $t^{\mathrm{n}+1}$. The first order CFEI scheme in [26, Remark 4.1] also shares a similar property.

The solutions to (37) are bounded independently of n and relative density ratio $\rho_s/\rho_f$. In other words, the coupled discrete fluid–structure system possesses energy functional that is bounded for all time, with the bound depending only on the problem data.

## 5. Numerical convergence and verification

In this section, we perform numerical simulations over two different problem setups: the first problem setup has been considered to access the temporal accuracy of the proposed CFEI scheme, whereas the second problem setup verifies the scheme with the FSI benchmark test cases given in [13]. Our numerical study focuses on 2D FSI problems for simplicity. However, the assessment of the stability and precision of the scheme can be generalized to 3D.
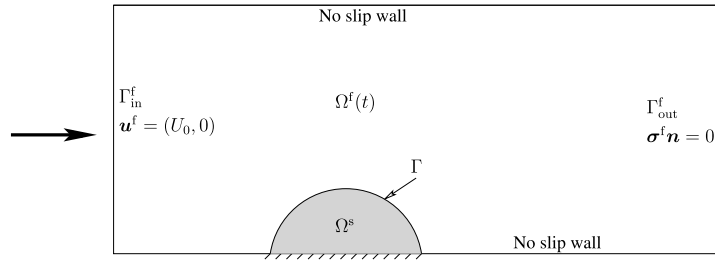
**Fig. 1.** Schematic and computational domain of elastic half-cylinder problem, and details of the boundary conditions.

### 5.1. Temporal accuracy

The objective of the first problem is to establish the temporal accuracy of the proposed CFEI scheme. The details of finite element implementation can be found in [36]. For this study, we consider a 2D laminar incompressible flow around a linearly elastic semi-circular cylinder of diameter $D$ fixed to the channel floor. Fig. 1 illustrates the problem schematics, where $\Omega^f(t)$ and $\Omega^s$ represent the fluid and solid domains, respectively and $\Gamma(t)$ defines the interface between the fluid and the solid domains. Here, we consider a rectangular domain of size $[0, 6.5] \times [-0.5, 1]$ with a deformable semi-circular cylinder of radius 0.5 centered at $z_0 = [1.5, -0.5]$ as the computational domain.

The above problem has been simulated using the following boundary conditions: (i) the inflow velocity has been prescribed on the boundary $\Gamma^f_{in}$ as $\boldsymbol{u}^f = (U_0, 0) = [g(t)(1 + 2y)(1 - y), 0]$. Further, the inflow velocity of the fluid has been assumed to be at rest for $t = 0$ and sinusoidally developing in time to attain the maximum value for $t = 2$. Therefore, the perturbation term $g(t)$ can be defined as $\frac{1}{2}[1 - \cos(\frac{\pi}{2}t)]$ for $t \leq 2$ and equal to 1 for $t > 2$. (ii) The no-slip boundary condition has been prescribed along the fluid–structure interface. (iii) Traction-free outflow boundary condition has been considered at the channel exit $\Gamma^f_{out}$ [37]. (iv) We assume the no-slip boundary condition for the fluid velocity at the side walls. For the semi-circular cylinder, we use the material properties: density $\rho^s = 1$, Lame's constants $\lambda^s = 500$ and $\mu^s = 50$. For the fluid we use density $\rho^f = 1$ and kinematic viscosity $\nu^f = 1$.

We simulate the aforementioned flow over semi-circular cylinder using the computational scheme presented in (37) for different time-step sizes of: $\Delta t = 1/40$, $1/80$, $1/120$, and $1/160$. The computational domain is discretized using the $\mathbb{P}_3/\mathbb{P}_2/\mathbb{P}_3$ higher order isoparametric finite elements for the fluid velocity, pressure and structural velocity, respectively. The fluid and solid meshes consist of 1239 and 370 triangular elements, respectively. All the numerical simulations for different time-step sizes are performed using the same initial reference mesh.

To demonstrate the temporal accuracy of the present scheme, we calculate the error in the computed solutions of the fluid velocity, pressure and the structural displacement for each of the time-step sizes specified above. Since a closed-form exact solution for this physical problem is not available, the numerical solutions for very small $\Delta t = 2 \times 10^{-5}$ have been considered as the reference solutions.

Fig. 2(a) shows the error for the interface position ($\|\boldsymbol{\varphi}^s(\boldsymbol{z}, 1) - \boldsymbol{\varphi}^s_h(\boldsymbol{z}, 1)\|_{\ell^2}$) at $t = 1$ with respect to the angle $\theta$, where $\theta = \theta(\boldsymbol{z})$ is the angle between $\boldsymbol{z} - \boldsymbol{z}_0$ and the positive $x$-axis. Figs. 2(b) and 3 report the errors in the structural velocity, the fluid velocity and the fluid pressure for various standard discrete norms, $L^\infty$, $L^2$, $H^1$, $W^{1,\infty}$. From these figures, it is evident that the lines plotted have a slope of $m = 2$, which clearly confirms the second-order accuracy of the CFEI scheme.

### 5.2. Numerical verification

Herein we present the verification of the CFEI solver before proceeding to study the flapping dynamics of a flexible elastic plate with a very low mass ratio. For this purpose, we simulate the cylinder-bar problem presented in [13]. One of the reasons for selecting this problem as a benchmark is its close resemblance with the proposed application discussed later. Fig. 4 depicts the problem definition and the details of the boundary conditions. A rectangular fluid domain $\Omega^f(t)$ of nondimensional length $L = 2.5$ and height $H = 0.41$ has been considered. The solid domain $\Omega^s$ consists of a stationary rigid cylinder positioned at $C = (0.2, 0.2)$ with radius $r = 0.05$ and a flexible elastic bar of length $l = 0.35$, thickness $h = 0.02$ attached to the rear of the cylinder. The boundaries of the flexible bar with the fluid domain forms the interface boundaries along which the momentum transfer takes place. All coordinates used in this problem are measured from the lower left-bottom corner of the domain which coincides with the origin of the Cartesian coordinate system used.

In this problem, the following boundary conditions have been considered: a parabolic velocity profile has been described at the inlet

$$\boldsymbol{u}^f = (U_0, 0) = \frac{6.0}{0.1641} g(t) \bar{U} y(0.41 - y), \tag{54}$$

where $\bar{U}$ denotes the mean inlet velocity. In this problem we assume that the inflow fluid is at rest for $t = 0$ and sinusoidally developing in time. Therefore, $g(t) = [1 - \cos(\frac{\pi}{2}\frac{t}{2})]$ for $t \leq 2$ and equals to unity for $t > 2$. The common boundary between the flexible bar and the fluid domain forms the fluid–structure interface. Traction-free outflow boundary condition has been
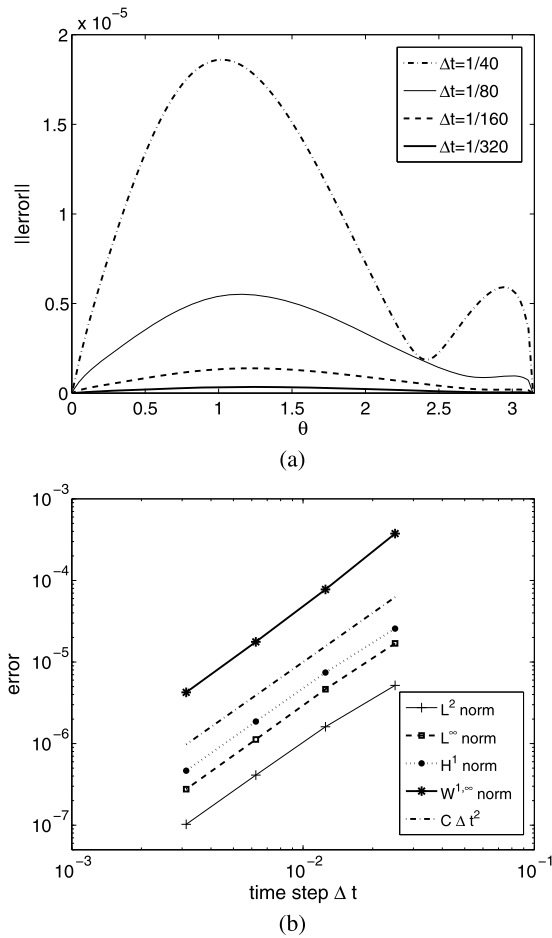
**Fig. 2.** Elastic half-cylinder problem: (a) error in position along the interface at $t = 1$, where $\|\boldsymbol{\varphi}^s(\boldsymbol{z}, 1) - \boldsymbol{\varphi}_h^s(\boldsymbol{z}, 1)\|_{\ell^2}$ versus $\theta$ and $\theta = \theta(\boldsymbol{z})$ is the angle between $(\boldsymbol{z} - z_0)$ and the positive $x$-axis. (b) 2nd order convergence of solid velocity in various norms.
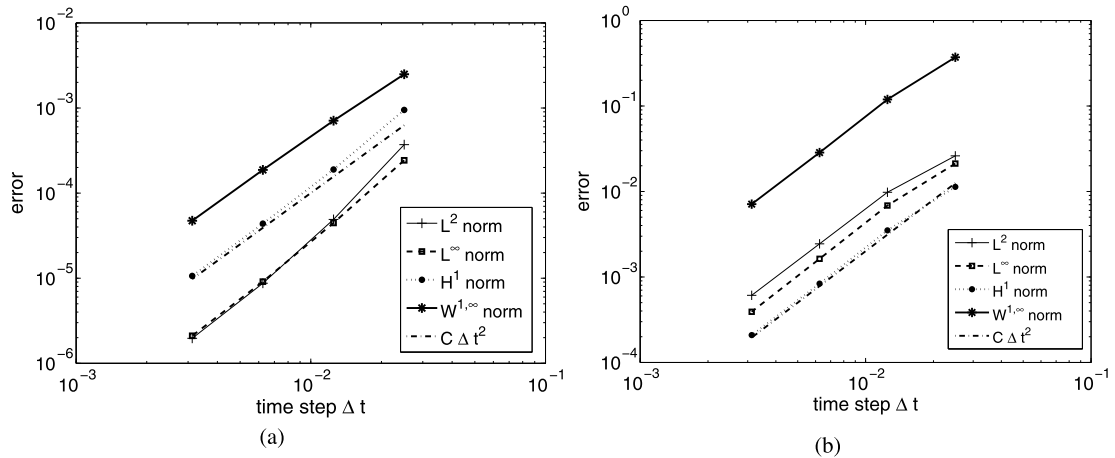


**Fig. 3.** Second order convergence in various norms at time $t = 1$ for fluid (a) velocity, (b) pressure.

considered at the channel exit $\Gamma_{\text{out}}^{\text{f}}$. The circular cylinder is assumed to be rigid and no-slip condition is considered at the cylinder surface and also along the sidewalls.

Assuming 2D laminar flow, we simulate this problem for three different FSI test cases described in [13]. Here, FSI-I is a steady state problem for $Re = 20$ and $\bar{U} = 0.2$, the nondimensional physical parameters for this test case are the ratio of structural density to fluid density $\rho^s/\rho^f = 1$, Poisson's ratio $\nu^s = 0.4$ and nondimensional Young's modulus $E/\rho^f \bar{U}^2 =$
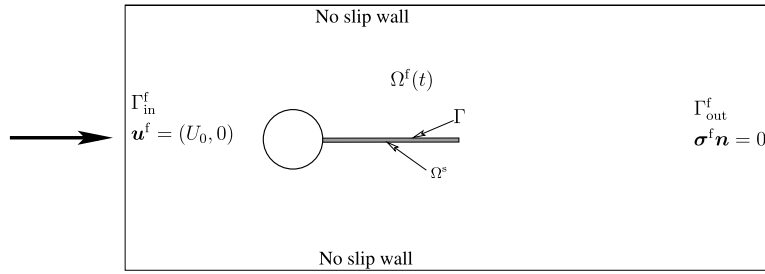
**Fig. 4.** Schematic and computational domain of cylinder-bar problem, and details of the boundary conditions and fluid–structure interface.

**Table 1**
FSI-I benchmark problem.

|  | Present computations | Benchmark results [13] |
|---|---|---|
| $\eta_x \times 10^{-3}$ | 0.0237 | 0.0227 |
| $\eta_y \times 10^{-3}$ | 0.842 | 0.821 |
| Drag | 14.23 | 14.27 |
| Lift | 0.748 | 0.763 |

$3.5 \times 10^4$. FSI-II and FSI-III are unsteady problems with oscillating flexible bar for $Re = 100$ and $Re = 200$, respectively. For FSI-II test case the nondimensional simulation parameters are $\rho^s/\rho^f = 10$, $\nu^s = 0.4$ and $E/\rho^f \bar{U}^2 = 1.4 \times 10^3$. Except for the Reynolds number and $\rho^s/\rho^f = 1$, identical nondimensional parameters have been used for FSI-III test case. The elastic flexible-bar has been modeled using the nonlinear St. Venant–Kirchhoff constitutive model defined in (6). Finally, to verify the CFEI scheme, we compare the values of forces and tip displacements with those reported by [13].

### 5.2.1. Steady flow past cylinder-bar problem at Re = 20 (FSI-I)

At $Re = 20$, the flow around a cylinder-bar assembly exhibits a steady state stability. The fluid and solid domain are discretized using $\mathbb{P}_2/\mathbb{P}_1/\mathbb{P}_2$ with total 2379 and 266 elements, respectively. For a constant $\Delta t = 0.005$ has been used for the computations. Table 1 compares the predicted results for the steady state problem with those reported in [13]. The present computations provide a good match with the reference data.

### 5.2.2. Unsteady cylinder-bar problem at Re = 100 and 200

The fluid and solid domains for $Re = 100$ problem are discretized using $\mathbb{P}_2/\mathbb{P}_1/\mathbb{P}_2$ triangular mesh consisting of 2379 and 266 elements, respectively. The problem $Re = 200$ uses a $\mathbb{P}_3/\mathbb{P}_2/\mathbb{P}_3$ discretization for the fluid domain with 2727 elements and the solid domain with 274 elements. A constant $\Delta t = 0.001$ has been considered for both the cases. We observe periodic oscillations for both $Re$. In addition, we also observe that the frequency of oscillation of drag force is twice that of lift force. Tables 2 and 3 show the computational results and the benchmark solutions given in [13] for $Re = 100$ and 200, respectively. The computed values are overall in good agreement with the benchmark solutions.

## 6. Application to flapping dynamics

In this section, we present an application of the presented CFEI scheme to simulate the flapping phenomena observed in a very thin flexible plate with low mass density ratio in a uniform axial flow. Through this application, we further demonstrate the numerical stability of the proposed scheme for low mass density ratio and show that the stability of the numerical scheme is independent of mass ratio. In this problem, we explore very low values of mass ratios, where the added mass effects are very strong and a small variation in the parameters can result in large change in the stability of the flapping dynamics. As a part of this study, we analyze the effects of the mass-ratio and the Reynolds number on the stability of flapping. To further verify the ability of the CFEI solver, we provide a comparison between the numerical simulations solutions and the analytical solutions [38]. The comprehensive study provides a better understanding of the physical mechanism associated with the flapping dynamics and the regime transitions.

We introduce the following nondimensional parameters to describe the dynamics involved in a flapping problem

$$m^* = \frac{\rho^s h}{\rho^f L}, \qquad K_B = \frac{EI}{\rho^f U_0^2 L^3 b}, \qquad Re = \frac{\rho^f U_0 L}{\mu^f}, \qquad H = \frac{h}{L}. \qquad (55)$$

Here, $m^*$ is the mass ratio of the flexible plate with the surrounding fluid, $K_B$ refers to the bending rigidity modulus, and $H$ is the ratio of thickness $h$ to the length $L$ of the plate, $I$ is the area moment of inertia of the rectangular plate defined as $bh^3/12(1 - \nu^2)$, $b$ is the width of the plate, $\nu$ denotes the Poisson's ratio and $E$ is the Young's modulus. The connection of the nondimensional parameters with the combined fluid–structure equations has been summarized in Appendix A.

**Table 2**
FSI-II benchmark problem.

| | Present computations | | Benchmark results | |
|---|---|---|---|---|
| | value | frequency | value | frequency |
| $\eta_x \times 10^{-3}$ | $-15.25 \pm 13.25$ | 3.8 | $-14.58 \pm 12.44$ | 3.8 |
| $\eta_y \times 10^{-3}$ | $1.30 \pm 82.70$ | 1.9 | $1.23 \pm 80.60$ | 2.0 |
| Drag | $214 \pm 77.566$ | 3.8 | $208 \pm 73.75$ | 3.8 |
| Lift | $1.01 \pm 235.96$ | 2.0 | $-0.88 \pm 234.20$ | 2.0 |

**Table 3**
FSI-III benchmark problem.

| | Present computations | | Benchmark results | |
|---|---|---|---|---|
| | value | frequency | value | frequency |
| $\eta_x [\times 10^{-3}]$ | $-2.90 \pm 2.75$ | 10.9 | $-2.69 \pm 2.53$ | 10.9 |
| $\eta_y [\times 10^{-3}]$ | $1.50 \pm 35.14$ | 5.5 | $1.48 \pm 34.38$ | 5.3 |
| Drag | $460.1 \pm 27.16$ | 10.9 | $457.3 \pm 22.66$ | 10.9 |
| Lift | $2.91 \pm 156.82$ | 5.5 | $2.22 \pm 149.78$ | 5.3 |



(a)



(b)
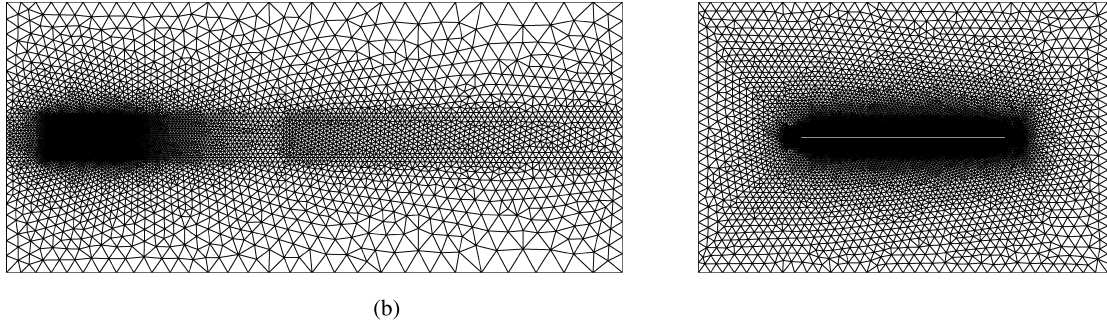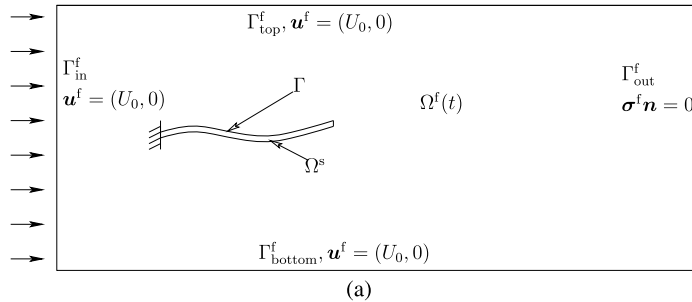
**Fig. 5.** Flapping dynamics problem: (a) schematic and computational domain with details of boundary conditions, (b) unstructured finite-element mesh corresponding to the flow domain with flexible plate at its undeformed configuration.

### 6.1. Problem description

The simulations are carried out on a two-dimensional thin flexible plate of length $L$ and thickness $h$, with its leading edge fixed and the trailing edge free to oscillate in the axial flow field. It is further considered that the thickness $h \ll L$, which makes the flexible plate into a very thin plate. In this study, the flexible plate has been modeled using the St. Venant–Kirchho material model given by (6). The effect of thickness on the stability has not been considered in this study.

Fig. 5(a) presents the details of the computational domain considered for this simulation study. The leading edge center is assumed to be the origin of the computational domain and the dimensions of the computational domain are $[-2L, 20L] \times [-5L, 5L]$. $\Gamma_{in}^f$ defines the inlet boundary with freestream velocity of $(\boldsymbol{u}^f = U_0, 0)$, the outlet $\Gamma_{out}^f$ is based on the traction-free outlet boundary, $\boldsymbol{n}\sigma^f = 0$ (see [37]), where $\boldsymbol{n}$ is the outward normal to the outlet boundary, $\Gamma_{top}^f$ and $\Gamma_{bottom}^f$ are the sides of the computational domain with freestream conditions $\boldsymbol{u}^f = (U_0, 0)$ and $\Gamma$ describes the common interface between the fluid and solid domains. All the physical parameters involved in this study are nondimensionalized considering $L$, $L/U_0$ and $\rho^f/L^3$ as the length, time and mass scales.

**Table 4**
Mesh convergence study at $m^* = 0.1$, $Re = 1000$ and $K_B = 0.0001$.

|                      | M1                                  | M2                                  | M3                       |
|----------------------|-------------------------------------|-------------------------------------|--------------------------|
| Nodes                | 14 773                              | 31 657                              | 61 154                   |
| Elements             | 7279                                | 15 699                              | 30 368                   |
| $\delta^{max}/L$     | $1.269 \times 10^{-1}$(4.62%)       | $1.212 \times 10^{-1}$(0.14%)       | $1.213 \times 10^{-1}$   |
| $\delta^{min}/L$     | $-1.278 \times 10^{-1}$(4.39%)      | $-1.235 \times 10^{-1}$(0.87%)      | $-1.225 \times 10^{-1}$  |
| $\Delta\delta/L$     | $2.550 \times 10^{-1}$(4.55%)       | $2.455 \times 10^{-1}$(0.67%)       | $2.439 \times 10^{-1}$   |
| $\delta^{rms}/L$     | $8.324 \times 10^{-2}$(1.66%)       | $8.403 \times 10^{-2}$(0.73%)       | $8.465 \times 10^{-2}$   |
| $C_l^{rms}$          | $8.614 \times 10^{-2}$(1.20%)       | $8.535 \times 10^{-2}$(0.28%)       | $8.512 \times 10^{-2}$   |



(a)                                                                (b)
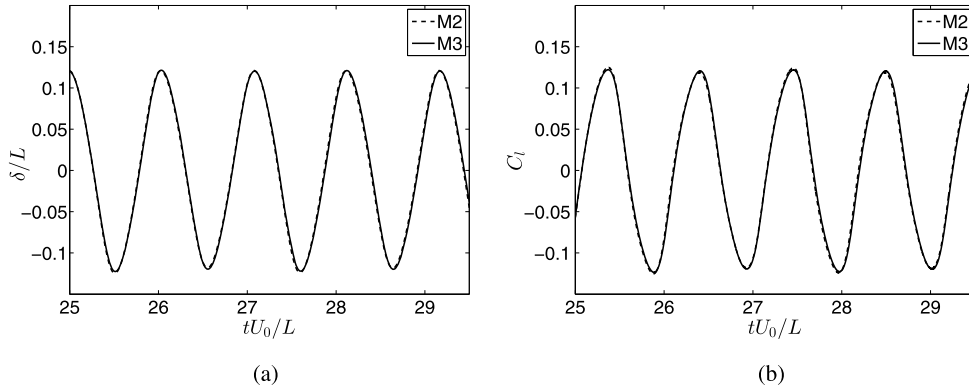
**Fig. 6.** Comparison of time history of (a) the tip-displacement and (b) the lift coefficient, $C_l$, over meshes-$M2$ and $M3$ for $m^* = 0.1$, $Re = 1000$ and $K_B = 0.0001$.



(a)                                                                (b)
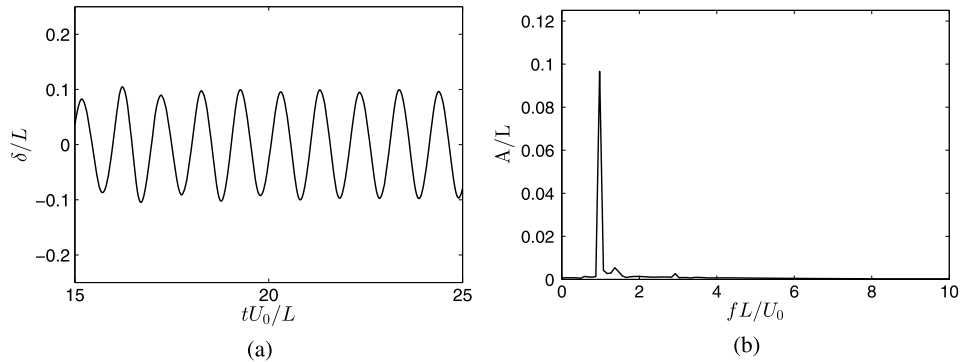
**Fig. 7.** Flapping response of the flexible plate at $Re = 1000$ (a) time history of cross-stream tail position response, (b) amplitude–frequency spectrum.

For the case of $Re = 1000$ and $m^* = 0.1$, three different meshes $M1$, $M2$ and $M3$ with increasing mesh resolutions are considered for a grid convergence study. Table 4 presents a detailed mesh statistics and Fig. 5(b) shows a representative unstructured fluid mesh $M3$ along with the close-up view of the mesh in the vicinity of the flexible plate. A suitable boundary layer mesh has been considered along the interface between the fluid and the flexible plate to capture the boundary layer development during flapping. For unsteady wake dynamics, a well resolved mesh has been considered in the wake region. The mesh convergence study has been performed using a constant time-step size $\Delta t = 0.001$ and the nondimensional parameters for the fluid and solid chosen are: $U_0 = 1$, $K_B = 0.0001$, and $H = 0.01$. A sinusoidally developing inlet flow has been considered for $t \in [0, 0.5]$. To assess the tip displacement and the force data, Table (4) provides the maximum, minimum, peak-to-peak and root-mean-square (RMS) tip displacement and the RMS lift coefficient values for the three meshes. We can observe from the table, the maximum difference between the meshes $M2$ and $M3$ is 0.87%. In addition, the time history of the trailing edge tip-displacement and the lift coefficient are shown in Fig. 6. Therefore, we believe the mesh $M2$ is sufficiently resolved and has been employed in this study of flapping dynamics.

### 6.2. Flapping dynamics and response study

In this section, we analyze the dynamic response of the flexible plate for $m^* = 0.075$, $Re = 1000$, $K_B = 0.0001$ and $H = 0.01$. Fig. 7(a) depicts the cross stream tip-displacement of the trailing edge for $tU_0/L \in [15, 25]$, which clearly shows
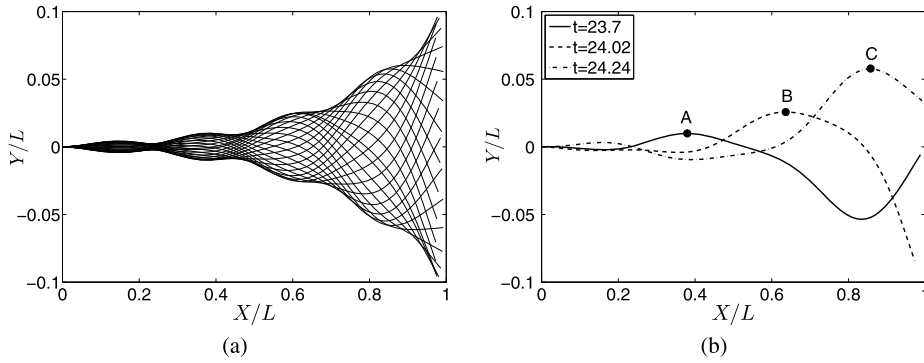
**Fig. 8.** Full body flapping response of the flexible plate at $Re = 1000$ and $K_B = 0.0001$ for (a) one complete oscillation cycle in $tU_0/L \in [24, 25]$ and (b) specific body position at $tU_0/L = 23.7, 24.02$ and $24.24$ to illustrate the traveling wave phenomenon.
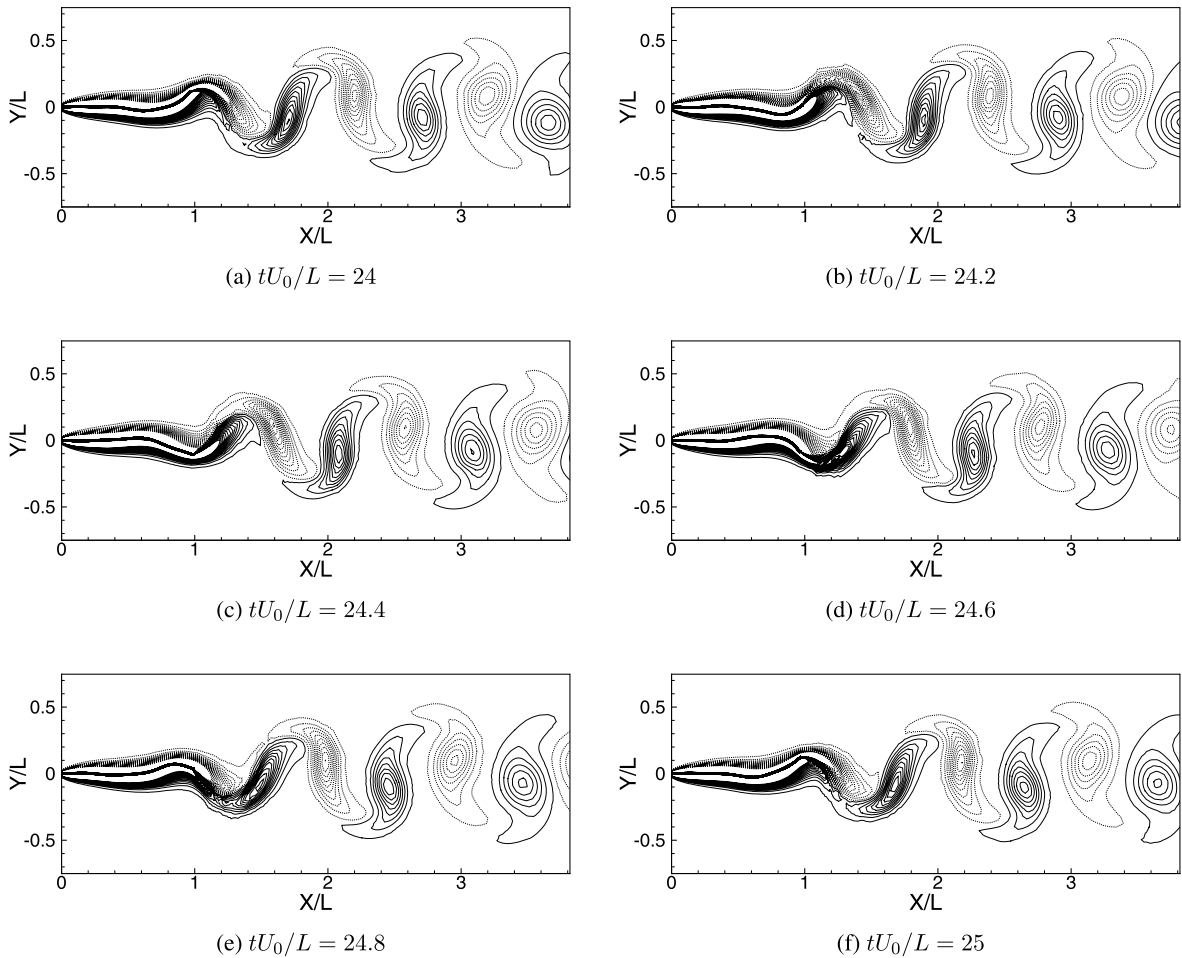


**Fig. 9.** Time series of body position and basic von Kármán vortex formation in the wake at $Re = 1000$ for $m^* = 0.075$ and $K_B = 0.0001$. Dashed lines indicate negative vorticity.

a regular sinusoidal time series with a single unique frequency. Moreover, Fig. 7(b) corroborates the observation of single unique frequency with the most dominant response frequency and amplitude of the tip-displacement response.

The full-body profile of the flexible plate has been plotted in Fig. 8(a) at various time instants of a complete cycle of oscillation. This illustrates the bottleneck mechanism observed experimentally earlier in [39] earlier. To illustrate further the existence of various modes of oscillation, we plot full body profiles at $tU_0/L = 23.7$, 24.02 and 24.24 in Fig. 8(b). The body profiles of the plate in Fig. 8(b) indicates a 3rd mode of oscillation. Interestingly, we observe that the point of maximum
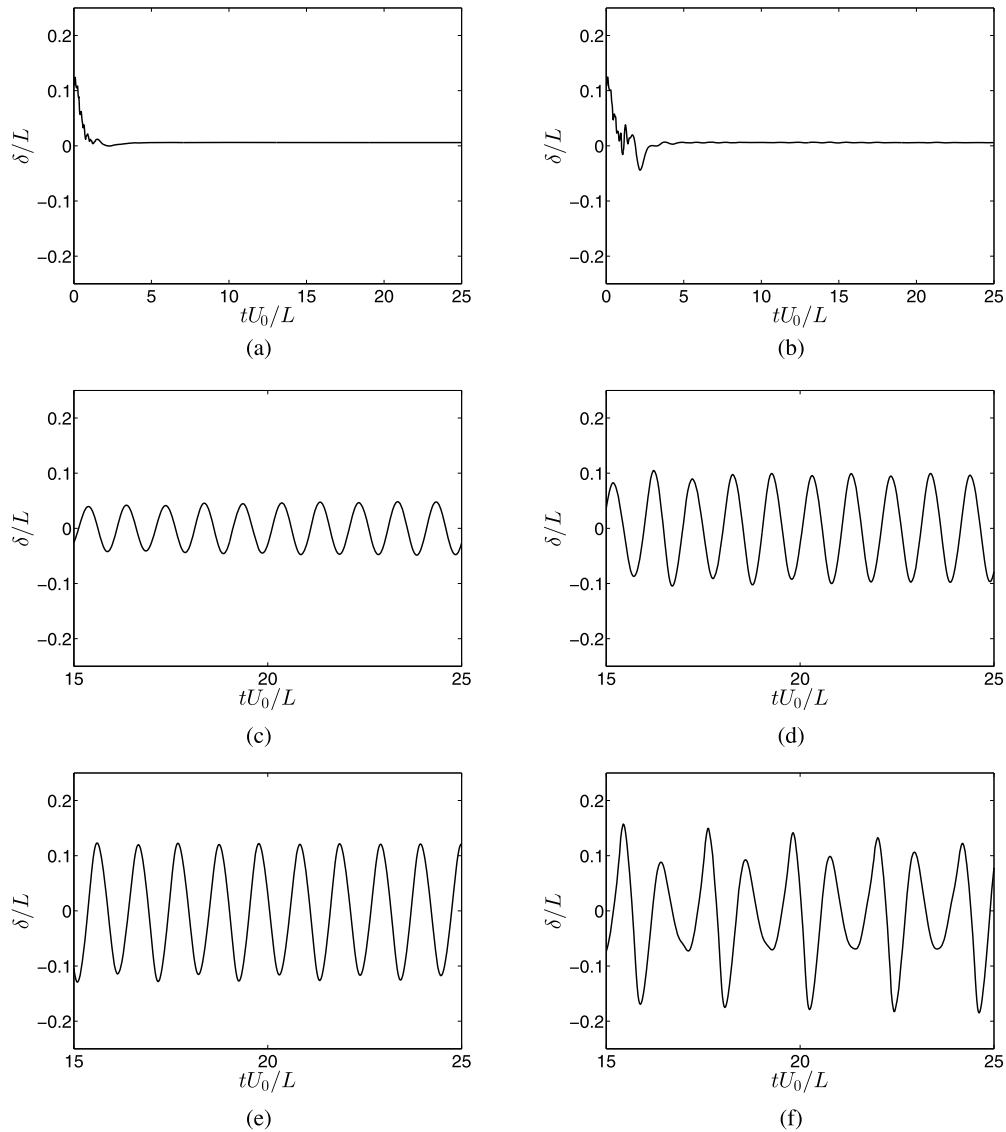
**Fig. 10.** Nondimensional cross-stream displacement histories of the trailing edge in axial flow at $Re = 1000$ for $K_B = 0.0001$ and $m^* = $ (a) 0.01, (b) 0.025, (c) 0.05, (d) 0.075, (e) 0.10 and (f) 0.125.

deformation, marked $A$, at $tU_0/L = 23.7$, travels downstream to point $B$ at $tU_0/L = 24.02$ and further downstream to $C$ at $tU_0/L = 24.24$. This explains the presence of a traveling wave in the flapping instability.

Fig. 9 shows instantaneous vorticity contours along the full-body profiles at distinct nondimensional time instants between 24 and 25 at $Re = 1000$. A pair of counter-rotating von Kármán vortices (2S) have been shed from the trailing edge for one complete oscillation of the flexible plate.

### 6.3. Effects of mass ratio

Next, we analyze the effects of mass ratio on the flapping dynamics at $Re = 1000$. The fluid and solid parameters considered for this study are: $K_B = 0.0001$, $H = 0.01$, $U_0 = 1$ with $m^*$ ranging between 0.01 and 0.2. To analyze the effect of mass ratio on the stability of the flexible plate in an axial flow, we introduce a small transverse perturbation of $0.1L$ at the tip of the plate.

Fig. 10 shows the time histories of nondimensional cross-stream displacement of the trailing edge for different $m^*$. From the cross-stream tip displacement curves shown in Fig. 10, it is clear that there exist three distinct regimes of response. For $m^* \leq 0.025$, the flexible plate stabilizes approximately to the fixed-stable position despite of initial disturbance. This regime is known as the fixed-point stability. For $m^* \geq 0.05$, the stream-wise tip displacement of the trailing edge does no longer stabilize to the stable-straight configuration. The mass ratio for at which the coupled system transitions from stable
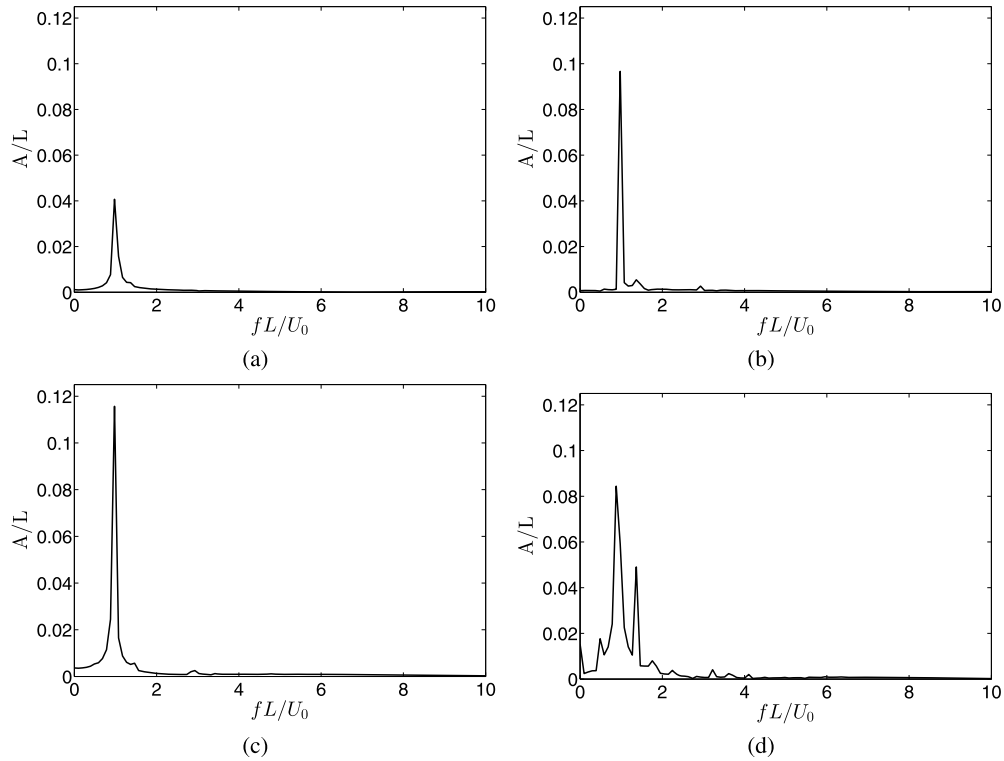
Fig. 11. Amplitude–frequency spectrum of the cross-stream displacement at $Re = 1000$ for $K_B = 0.0001$ and $m^* =$ (a) 0.05, (b) 0.075, (c) 0.10 and (d) 0.125.
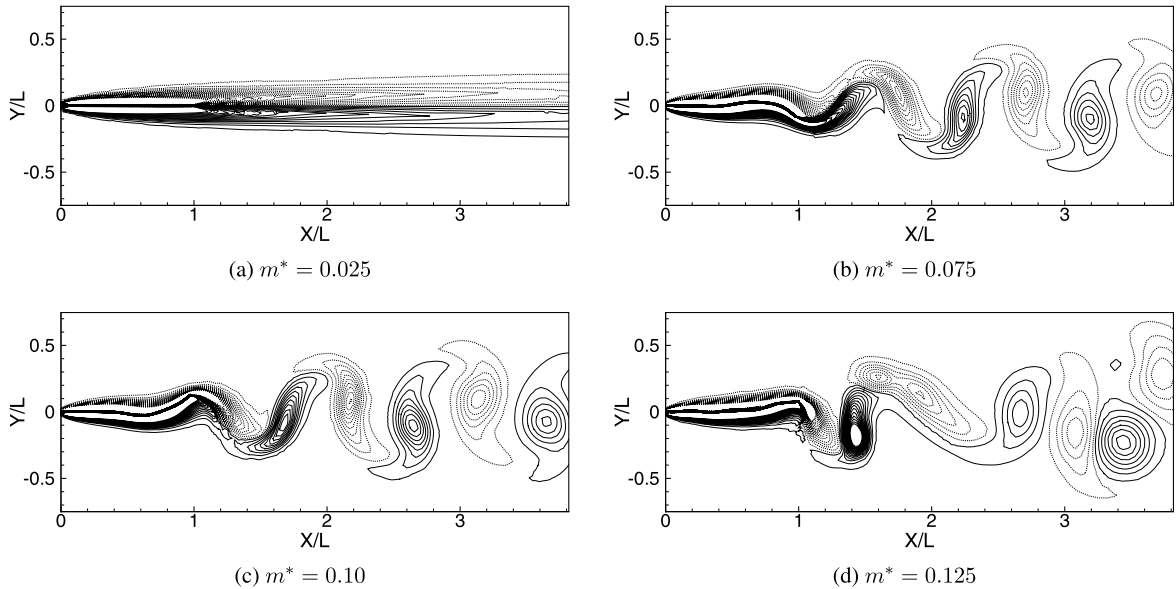


Fig. 12. Instantaneous vorticity contours at $tU_0/L = 25$ in the wake for different mass-ratios at $Re = 1000$ for $K_B = 0.0001$. Dashed lines denote the negative vorticity.

to oscillating behavior is defined as critical mass ratio $m_{cr}^*$. This phenomenon of transition from stability was also observed experimentally [39]. We also observe that the time histories of the tip displacement for $0.05 \leq m^* \leq 0.1$ characterize a regular sinusoidal oscillations with a single dominant frequency. This range of mass ratios belongs to the limit-cycle flapping regime. For the mass ratios $m^* \geq 0.125$ characterize non-periodic tip displacement and this regime is referred to as chaotic flapping. To further analyze the tip displacement, we plot the amplitude–frequency spectrum in Fig. 11 for a range of $m^*$ between 0.05 and 0.125. A single unique frequency $f_1 = 0.97656$ characterizes the limit cycle flapping regime ($0.05 \leq m^* \leq 0.1$), whereas the chaotic flapping regime is associated with multiple frequencies ($m^* \geq 0.125$).
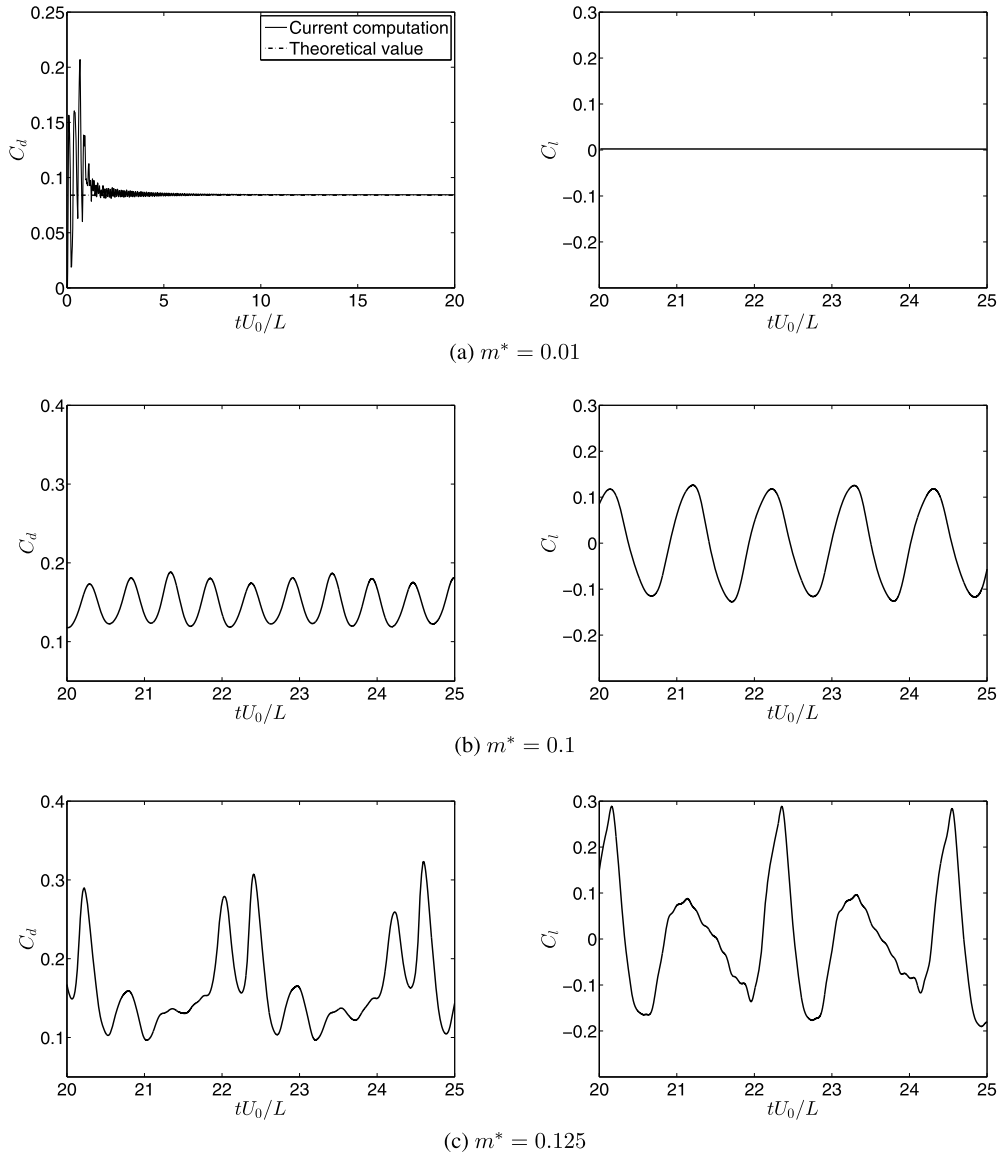
**Fig. 13.** Time histories of the drag (left) and lift coefficients (right) at $Re = 1000$ for $K_B = 0.0001$ and $m^* =$ (a) 0.01, (b) 0.1, and (c) 0.125.

Fig. 12 plots the instantaneous vorticity contours in each of the three stability regimes. For $m^*$ corresponding to the fixed-stable flapping regime, a narrow and steady wake is observed marked by no oscillation in the wake vortices. A periodic 2S von Kármán vortex pattern is observed for $m^* = 0.075$ and $m^* = 0.1$ for the limit-cycle flapping regime. A non-periodic vortex street is seen for the chaotic flapping regime as the mass ratio $m^*$ increases to 0.125.

We further examine the characteristics of fluid-dynamic force coefficients for the three flapping stability regimes. Fig. 13 shows the time series of drag coefficient $C_d$ and lift coefficient $C_l$ for $m^* = 0.025$, 0.1 and 0.125 for $Re = 1000$, $K_B = 0.0001$ and $t \in [15, 20]$. For $m^* = 0.025$ (fixed-point stability), as shown in Fig. 13(a), it can be seen that the drag coefficient $C_d$ converges to 0.084, which is equal to the value of $C_d$ for a flat plate at zero degree incidence obtained from the classical boundary layer theory. As apparent from Fig. 13(b), $C_d$ and $C_l$ are periodic in the limit-cycle oscillation regime for $m^* = 0.1$. Further, one can also observe for $m* = 0.125$ $c_d$ and $c_l$ are non-periodic.

## 6.4. Effects of Reynolds number

With regard to time evolution, Fig. 14 presents a comparison of the cross-stream tip displacement at $Re = 500$, 750 and 1000 with $K_B = 0.0001$ and $m^* = 0.1$. With increasing $Re$, the system leads to either a limit-cycle or a chaotic flapping mode. The maximum amplitude of cross-stream tip displacement increases with increasing $Re$. The stability of the system at lower $Re$ can be explained by the stabilizing effect of the tension induced due to the viscous shear stresses [38].
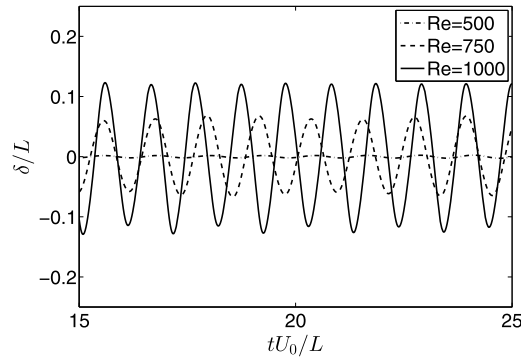
**Fig. 14.** Evolution of cross-stream displacement at $Re = 500, 750$ and $1000$ with $m^* = 0.10$, $K_B = 0.0001$.
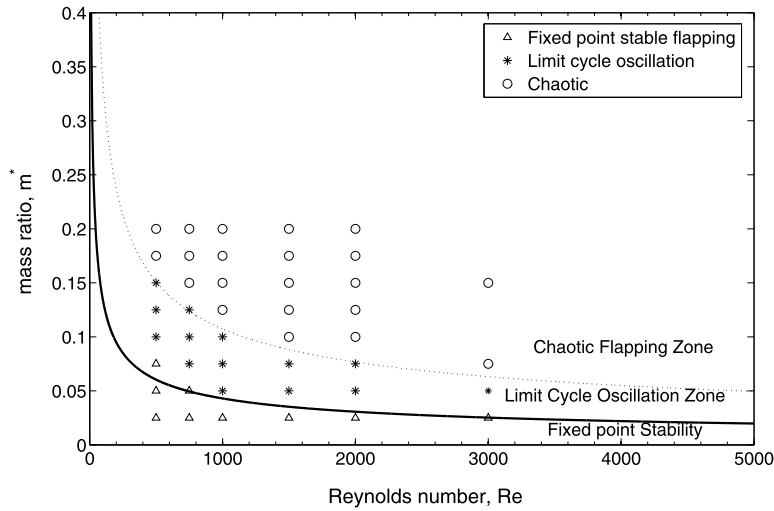


**Fig. 15.** Stability phase diagram for Reynolds Number $Re$ versus $m^*$. The plot is divided into three parts by $m_{cr}^*$ and $m_{chaotic}^*$ defined by (56). $m_{cr}^*$ curve is given by (−) and $m_{chaotic}^* = 2.5 \times m_{cr}^*$ curve is indicated by (···).

### 6.5. Stability regime map

The nonlinear stability results of flapping dynamics can be summarized in Fig. 15 with the aid of $Re$–$m^*$ diagram. The diagram shows various stability zones observed computationally using the CFEI scheme by changing the mass density ratio and $Re$. We have considered a reasonably large number of mass ratios for the detailed investigation. The diagram shows the three distinct regimes of stability: (i) fixed-point stability, (ii) limit-cycle flapping, and (iii) chaotic flapping. The curves for transition from stable to limit-cycle and the transition to chaos are also plotted in Fig. 15. For completeness, the linear stability analysis for the flexible plate in axial flow is summarized briefly in Appendix B. The theoretical expression (see Appendix B) for $m_{cr}^*$ for transition from fixed-point stability to limit-cycle flapping can be given by

$$m_{cr}^* = C_T Re^{-1/2} + K_B \pi^2, \tag{56}$$

where the induced tension coefficient $C_T = 1.328$, wave number $k_x = \pi$ in (B.8). We find a reasonable fit of the numerical predictions of critical mass ratio with the theoretical transition curves given by (56). As the mass ratio is increased, the wake of fixed-point becomes a limit cycle with alternate shedding of vortices in the wake. As the mass ratio is increased further, the wake is characterized by the non-periodic vortex patterns.

## 7. Conclusions

The present contribution was concerned with the design of a second-order CFEI algorithm for FSI. The method is based upon the arbitrary Lagrangian–Eulerian and finite element procedures. A mathematical analysis was performed for the stability of the CFEI scheme. The analysis has shown that the CFEI scheme possess energy functionals that are bounded for all time, with the bound independent of structure-to-fluid mass ratio. Second-order temporal accuracy of the scheme has been confirmed through a systematic analysis. The coupled fluid–structure results are verified with the reference benchmark data.

We have further assessed the numerical stability of the proposed order second-order method by simulating the flapping motion of a thin flapping body in a uniform flow with strong added-mass effects. Through our direct fluid–structure simulations, we have studied the flapping results for a wide range of mass ratios and varying Reynolds numbers while maintaining relatively low bending rigidity. As a function of mass ratio, the flapping dynamics reveals three distinct regimes: fixed-point stability, limit-cycle flapping, and chaotic flapping. The changes associated with regime transition with increasing mass ratio were analyzed by vortex wake patterns, tip displacements, and drag-lift coefficients. Dependencies of stability predicted by the linear analysis are confirmed by the nonlinear fluid–structure simulations. The presented method can be easily extended to three-dimensional without any loss of generality, only requiring larger computational load.

## Acknowledgements

## Appendix A. Nondimensionalization of combined fluid–structure equations

Nondimensionalizing the governing equations (1) and (9) by introducing the length, velocity and time scales as

$$L_{\text{ref}} = L, \quad U_{\text{ref}} = U_0, \quad T_{\text{ref}} = L/U_0.$$

The nondimensional parameters are written as

$$\nabla \boldsymbol{u}^{\text{f}'} = U_0/L \nabla \boldsymbol{u}^{\text{f}}, \qquad \nabla \boldsymbol{\varphi}^{\text{s}'} = \nabla \boldsymbol{\varphi}^{\text{s}}, \quad \boldsymbol{u}^{\text{f}'} = \boldsymbol{u}^{\text{f}}/U_0 \tag{A.1}$$

where $(\cdot)'$ denotes the nondimensional quantities. Nondimensional form of the governing equations using the nondimensional parameters in (55) and scaling parameters, (A.1) can be written as:

$$\frac{\partial \boldsymbol{u}^{\text{f}}}{\partial t} + \boldsymbol{u}^{\text{f}} \cdot \nabla \boldsymbol{u}^{\text{f}} = \nabla \cdot \boldsymbol{\sigma}^{\text{f}} + \rho^{\text{f}} \boldsymbol{g}^{\text{f}} \quad \text{in } \Omega^{\text{f}}(t), \tag{A.2}$$

$$m^* \frac{\partial^2 \boldsymbol{\varphi}^{\text{s}}}{\partial t^2} = \nabla \cdot \boldsymbol{\sigma}^{\text{s}} + H \boldsymbol{f}^{\text{s}} \quad \text{in } \Omega^{\text{s}}(t), \tag{A.3}$$

where

$$\boldsymbol{\sigma}^{\text{f}} = -p\mathbf{I} + \frac{1}{Re}\left[\nabla \boldsymbol{u}^{\text{f}} + \left(\nabla \boldsymbol{u}^{\text{f}}\right)^T\right], \tag{A.4}$$

$$\boldsymbol{\sigma}^{\text{s}} = \frac{12 K_{\text{B}}}{H^2}(1-\nu)\boldsymbol{F}\boldsymbol{E} + \frac{12 K_{\text{B}}}{H^2}\frac{\nu(1-\nu)}{(1-2\nu)}(\text{tr } \boldsymbol{E})\boldsymbol{F} \tag{A.5}$$

where $\nu$ refer to the Poisson's ratio of the flexible beam. $\boldsymbol{E}$ and $\boldsymbol{F}$ define strain tensor (see (7)) and the deformation gradient tensor, respectively. $(\cdot)'$ notation for nondimensional quantities is dropped for brevity.

## Appendix B. Linear stability analysis for flexible plate in axial flow

In this section, we perform the linear stability analysis for the flexible plate of length $L$ in an axial free with velocity $U_0$. For more details about linear stability analysis of a flexible plate in axial flow refer [38]. In this analysis, the thickness of the plate assumed to be negligibly small compared to plate length. For the purpose of stability analysis, we introduce a small disturbance and consider that the propagation of this disturbance can be represented using a traveling wave. The wave dispersion for the flexible plate system in an incompressible axial flow is given by

$$\begin{aligned} D(k_x, \omega) = {} & \frac{Eh^3}{12(1-\nu^2)}k_x^4 - \rho^{\text{s}}h\omega^2 + C_{\text{T}}U_0^2 Re^{-1/2}L k_x^2 \\ & - 2\rho^{\text{f}}\left[\frac{(\omega - U_0 k_x)^2}{|k_x|} + i2\nu k_x^2 \frac{(\omega - U_0 k_x)}{|k_x|}\right]. \end{aligned} \tag{B.1}$$

where $k_x$, $\omega$ represent the wave number and frequency, $Re$ is the Reynolds number, $E$ and $\nu$ define the Young's modulus and Poisson's ratio, respectively. For detailed derivation of the above dispersion equation refer to [38]. Here we consider that the tension coefficient $C_{\text{T}} = 1.328$, which is a more conservative approximation for tension induced in the flexible plate due to viscous drag than the average tension coefficient introduced in [38].

Nondimensionalizing the dispersion equation (B.1), the length, velocity and time scales are

$$L_{\text{ref}} = L, \qquad U_{\text{ref}} = U_0, \qquad t_{\text{ref}} = L/U_0. \tag{B.2}$$

Substituting the nondimensional parameters described in (55) and additional the nondimensional quantities as

$$k_x' = k_x L_{\text{ref}}, \qquad \omega' = \omega L/U_0 \quad \text{and} \quad \nu' = \nu \frac{t_{\text{ref}}}{L_{\text{ref}}^2},$$ (B.3)

we obtain from (B.1)

$$D(k_x, \omega) = \frac{EI}{U_0^2 b \rho^f L^3} k_x^4 - m^* \omega^2 + C_T Re^{-1/2} k_x^2$$
$$- 2 \left[ \frac{(\omega - k_x)^2}{|k_x|} + i 2\nu k_x^2 \frac{(\omega - k_x)}{|k_x|} \right].$$ (B.4)

Neglecting the complex component and rewriting the dispersion relation (B.4) as a quadratic equation in $\omega$ will lead to

$$(m^* + 2/k_x)\omega^2 - 4\omega - C_T Re^{-1/2} k_x^2 + 2k_x - K_B k_x^4 = 0$$ (B.5)

The dispersion relation (B.4) of the coupled axial flow and the flexible plate system exhibit temporal instability for all negative imaginary components of $\omega$. Therefore, the condition for the system to be unstable is

$$4m^* \left( C_T Re^{-1/2} k_x - 2 + K_B k_x^3 \right) + 8 \left( C_T Re^{-1/2} + K_B k_x^2 \right) < 0.$$ (B.6)

From (B.6), the thin flexible plate exhibits transition from stability for mass-ratios

$$m^* > \frac{C_T Re^{-1/2} + K_B k_x^2}{1 - C_T Re^{-1/2} k_x/2 - K_B k_x^3/2}$$ (B.7)

A conservative approximation for the minimum mass-ratio can be described by simplifying (B.7) as

$$m^*_{cr} = C_T Re^{-1/2} + K_B k_x^2$$ (B.8)

# References

[1] J.R. Cebral, R. Lohner, Conservative load projection and tracking for fluid–structure problems, AIAA J. 35 (1997) 687–692.
[2] R. Jaiman, P. Geubelle, E. Loth, X. Jiao, Transient fluid–structure interaction with non-matching spatial and temporal discretizations, Comput. Fluids 50 (2011) 120–135.
[3] L. Huang, Flutter of cantilevered plates in axial flow, J. Fluids Struct. 2 (1995) 127–147.
[4] C.S. Peskin, The immersed boundary method, Acta Numer. 11 (2002) 479–517.
[5] R. Jaiman, F. Shakib, O.H. Oakley, Y. Constantinides, Fully coupled fluid–structure interaction for offshore applications, in: ASME Offshore Mechanics and Arctic Engineering OMAE09-79804 CP, 2009.
[6] R. Jaiman, Advances in ALE based fluid–structure interaction modeling for offshore engineering applications, in: 6th European Congress on Computational Methods in Applied Sciences and Engineering (ECCOMAS 2012), Vienna, 2012.
[7] M. Arienti, P. Hung, E. Morano, E. Shepherd, A level set approach to Eulerian–Lagrangian coupling, J. Comput. Phys. 185 (2003) 213–251.
[8] R.J. LeVeque, Z. Li, Immersed interface methods for stokes flow with elastic boundaries, SIAM J. Sci. Comput. 18 (1997) 709–735.
[9] R. Glowinski, T.W. Pan, J. Periaux, A fictitious domain method for external incompressible viscous flow modeled by Navier–Stokes equations, Comput. Methods Appl. Mech. Eng. 112 (1994) 133–148.
[10] R.P. Fedkiw, Coupling an Eulerian fluid calculation to a Lagrangian solid calculation with the ghost fluid method, J. Comput. Phys. 175 (2002) 200–224.
[11] J. Donea, S. Giuliani, J.P. Halleux, An arbitrary Lagrangian–Eulerian finite element method for transient dynamic fluid–structure interactions, Comput. Methods Appl. Mech. Eng. 33 (1982) 689–723.
[12] J. Liu, Simple and efficient ALE methods with provable temporal accuracy up to fifth order for the Stokes equations on time varying domains, SIAM J. Numer. Anal. 51 (2013) 743–772.
[13] J. Hron, S. Turek, A Monolithic FEM/Multigrid Solver for an ALE Formulation of Fluid–Structure Interaction with Applications in Biomechanics, Springer, 2006.
[14] M. Heil, A.L. Hazel, J. Boyle, Solvers for large-displacement fluid–structure interaction problems: segregated versus monolithic approaches, Comput. Mech. 43 (2008) 91–101.
[15] A. Robinson-Mosher, C. Schroeder, R. Fedkiw, A symmetric positive definite formulation for monolithic fluid structure interaction, J. Comput. Phys. 230 (2011) 1547–1566.
[16] F. Gibou, C. Min, Efficient symmetric positive definite second-order accurate monolithic solver for fluid/solid interactions, J. Comput. Phys. 231 (2012) 3246–3263.
[17] C.A. Felippa, K.C. Park, C. Farhat, Partitioned analysis of coupled mechanical systems, Comput. Methods Appl. Mech. Eng. 190 (2001) 3247–3270.
[18] H.G. Matthies, R. Niekamp, J. Steindorf, Algorithms for strong coupling procedures, Comput. Methods Appl. Mech. Eng. 195 (2006) 2028–2049.
[19] R. Jaiman, P. Geubelle, E. Loth, X. Jiao, Combined interface condition method for unsteady fluid–structure interaction, Comput. Methods Appl. Mech. Eng. 200 (2011) 27–39.
[20] C. Farhat, K.G. van der Zee, P. Geuzaine, Provably second-order time-accurate loosely-coupled solution algorithms for transient nonlinear computational aeroelasticity, Comput. Methods Appl. Mech. Eng. 195 (2006) 1973–2001.
[21] F.J. Blom, A monolithical fluid–structure interaction algorithm applied to the piston problem, Comput. Methods Appl. Mech. Eng. 167 (1998) 369–391.
[22] C. Michler, E.H. van Brummelen, S.J. Hulshoff, R. de Borst, The relevance of conservation for stability and accuracy of numerical methods for fluid–structure interaction, Comput. Methods Appl. Mech. Eng. 192 (2003) 4195–4215.
[23] S. Piperno, C. Farhat, Partitioned procedures for the transient solution of coupled aeroelastic problems part 1: model problem, theory, and two-dimensional application, Comput. Methods Appl. Mech. Eng. 124 (1995) 79–112.
[24] P. Causin, J.F. Gerbeau, F. Nobile, Added-mass effect in the design of partitioned algorithms for fluid–structure problems, Comput. Methods Appl. Mech. Eng. 194 (2005) 4506–4527.

[25] E.H. van Brummelen, Added mass effects of compressible and incompressible flows in fluid–structure interaction, J. Appl. Mech. 76 (2009) 021206.
[26] J. Liu, Combined field formulation and a simple stable explicit interface advancing scheme for fluid structure interaction, manuscript, available at http://arxiv.org/abs/1401.0082.
[27] S.O. Unverdi, G. Tryggvason, A front-tracking method for viscous, incompressible, multi-fluid flows, J. Comput. Phys. 100 (1992) 25–37.
[28] M.A. Fernández, J.-F. Gerbeau, C. Grandmont, A projection semi-implicit scheme for the coupling of an elastic structure with an incompressible fluid, Int. J. Numer. Methods Eng. 69 (2007) 794–821.
[29] A. Masud, T.J.R. Hughes, A space-time Galerkin/least-square finite element formulation of the Navier–Stokes equations for moving domain problems, Comput. Methods Appl. Mech. Eng. 146 (1997) 91–126.
[30] R. Jaiman, X. Jiao, P. Geubelle, E. Loth, Assessment of conservative load transfer on fluid-solid interface with nonmatching meshes, Int. J. Numer. Methods Eng. 64 (2005) 2014–2038.
[31] R. Temam, Navier–Stokes Equations. Theory and Numerical Analysis, AMS Chelsea Publishing, 2001.
[32] E. Weinan, Jian-Guo Liu, Projection method III: spatial discretization on the staggered grid, Math. Comput. 71 (237) (2002) 27–47.
[33] J.-G. Liu, J. Liu, R.L. Pego, Stable and accurate pressure approximation for unsteady incompressible viscous flow, J. Comput. Phys. 229 (2010) 3428–3453.
[34] A. Quarteroni, A. Valli, Numerical Approximation of Partial Differential Equations, Springer-Verlag, Berlin, 1994.
[35] S.C. Brenner, R. Scott, The Mathematical Theory of Finite Element Methods, 2nd edition, Springer-Verlag, 2002.
[36] L. Chen, C.-S. Zhang, A coarsening algorithm on adaptive grids by newest vertex bisection and its application, J. Comput. Math. 28 (2010) 767–789.
[37] J. Liu, Open and traction boundary conditions for the incompressible Navier–Stokes equations, J. Comput. Phys. 228 (2009) 7250–7267.
[38] R. Jaiman, M.K. Parmar, P.S. Gurugubelli, Added mass and aeroelastic stability of a flexible plate interacting with mean flow in a confined channel, J. Appl. Mech. 81 (2013).
[39] Y. Watanabe, S. Suzuki, M. Sughihara, Y. Sueoka, An experimental study of paper flutter, J. Fluids Struct. 16 (2002) 529–542.